Planetary Simulations Using the Wisdom–Holman Integrator: Large Time Steps and Resonances

by

J.F.F. Jonkers

July 2025

Bachelor Thesis
Bachelor of Science in Applied Physics and Applied Mathematics
Delft University of Technology

Abstract

The long-term simulation of planetary systems poses significant challenges due to the inherently chaotic and non-integrable nature of gravitational interactions in the N-body problem. This thesis examines the Wisdom–Holman symplectic integration scheme, a method specifically designed for nearly integrable systems. This scheme separates the dominant Keplerian motion from weaker perturbative forces, enabling stable integration over astronomical timescales. Emphasis is placed on understanding the practical limitations and capabilities of this method when using large time steps, particularly in the presence of mean-motion resonances and step-size resonances. Through extensive numerical experiments using the Rebound simulation package, the scaling behavior of integration errors is characterized, revealing a transition from second-order to lower-order error regimes at large time steps. This shows that in certain systems, time steps significantly larger than the shortest orbital period can still yield acceptable accuracy. However, in systems with mean-motion resonance, strong sensitivity to step-size resonances is observed, requiring careful step-size selection. A comparison between Jacobi and Democratic Heliocentric coordinates shows that the former performs best when orbits are nested, while the latter is better suited to systems with crossing or unordered orbits. These findings provide practical guidelines for applying Wisdom–Holman integration effectively across a range of dynamical regimes.

Supervisors:
Dr. P.M. Visser (TU Delft, Faculty of Electrical Engineering, Mathematics & Computer Science)
Prof. Dr. S. Stallinga (TU Delft, Faculty of Applied Sciences)

Contents

1 Introduction

Predicting the long-term evolution of planetary systems is one of the most challenging problems in celestial mechanics. While the two-body problem can be solved exactly, adding just one more gravitationally interacting body renders the system non-integrable in general, giving rise to complex dynamical features such as chaos, resonances, and sensitive dependence on initial conditions [1]. This inherent unpredictability over long timescales means that numerical simulations are essential for studying the stability and evolution of multi-body systems such as our Solar System, exoplanetary systems, and asteroid belts.

In recent years, the need for accurate and efficient orbital simulations has become increasingly important. A well-known example is the occasional appearance of alarming predictions in the news about near-Earth asteroids that could potentially collide with Earth in the future. While further refined calculations almost always rule out such impacts, for instance, the asteroid 2023 DW initially caused concern when preliminary estimates suggested a non-negligible chance of impact [2], these cases highlight the delicate interplay between initial condition uncertainty and orbital dynamics. Tiny uncertainties in position and velocity can lead to significantly different outcomes over decades or centuries, especially when chaotic regions of phase space or resonances are involved.

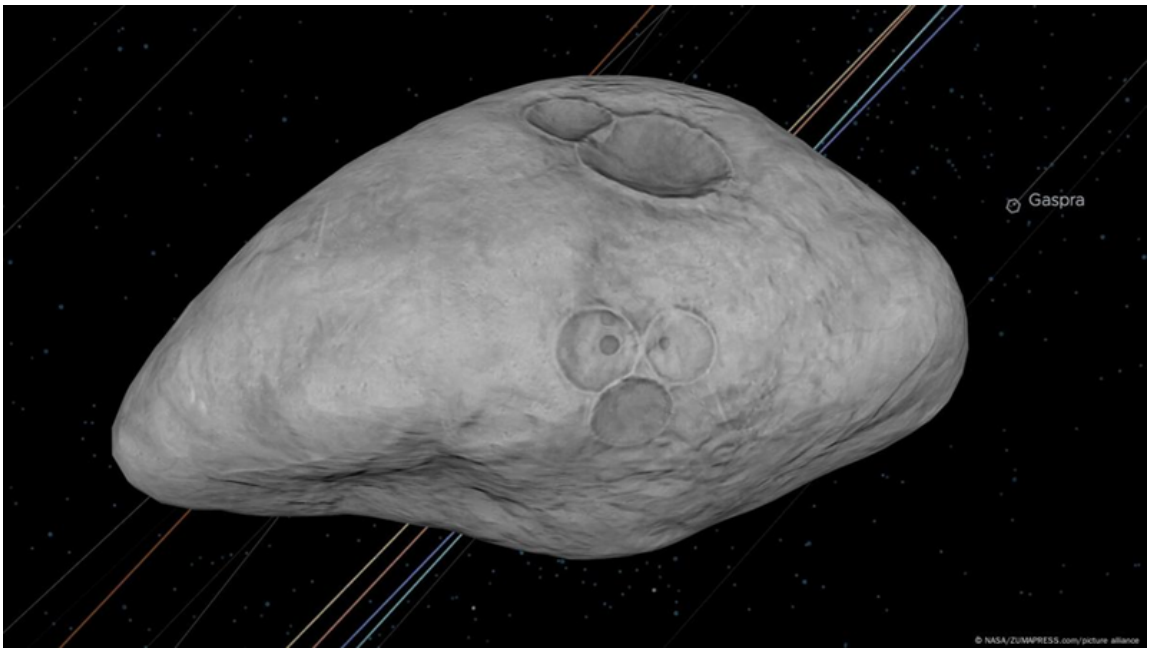

Figure 1: An artist's impression of the asteroid 2023 DW, where simulations at first suggested a non-negligible chance of a future impact with the Earth.

This uncertainty calls for not just a single simulation with the "best guess" initial conditions, but rather for large ensembles of simulations to characterize possible trajectories and impact probabilities statistically. However, running millions of high-precision, small-step integrations for each

possible variation in starting conditions is computationally prohibitive, even with modern supercomputers. This is where fast but reliable numerical integrators come in. If each individual simulation can be performed orders of magnitude faster without sacrificing the essential dynamical fidelity, then the entire ensemble study becomes feasible. This is not only useful in the context of asteroid impacts, but also in the study of exoplanetary system formation and stability, where the ability to simulate using many different initial conditions quickly would be invaluable.

Symplectic integrators, particularly the Wisdom–Holman scheme introduced in 1991 [3], play a crucial role here. The Wisdom-Holman method leverages the fact that many planetary systems are near-integrable, meaning they can be well-described as a dominant Keplerian (two-body) motion around a central body perturbed by relatively weak interactions. By splitting the Hamiltonian into an exactly solvable Keplerian part and a numerically integrated perturbative part, the Wisdom-Holman method preserves the system's symplectic structure, ensuring that energy errors do not drift systematically over long timescales. This allows the use of much larger time steps than would be possible with generic methods such as Runge–Kutta, without losing the crucial qualitative dynamics of the system.

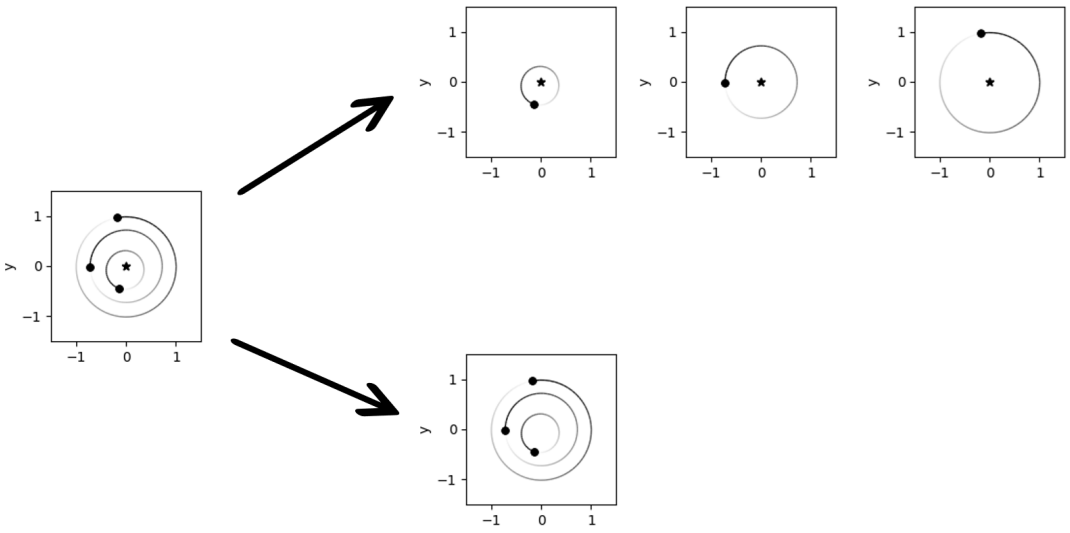

Figure 2: An illustration behind the idea of a Wisdom-Holman integration scheme. The total system is split up into two parts; The analytical Kepler orbits of the bodies around the central mass, and the interaction between the bodies themselves.

An efficient integration scheme which could perform long term simulations while also taking into account close encounters could be made by merging the Wisdom-Holman integrator (which accurately captures long term perturbative effects) with the Visser collision detection algorithm [4] (which can use Kepler orbits around a central mass to predict collision or close encounters between bodies, but doesn't capture long term perturbative effects)

The Wisdom-Holman method can't be used in cases where close encounters between bodies occur, as in such cases, the perturbation becomes of the same order or even higher than the analytical Kepler part. However, the Visser collision detection algorithm [4] presents a robust and efficient method for detecting close encounters and actual collisions in N-body simulations using the bodies Kepler orbits. Combining this kind of algorithm with a Wisdom–Holman integrator would enable high-fidelity, long-term simulations of densely populated systems such as asteroid belts or planetary ring systems, where both orbital evolution due to perturbative effects (captured by the Wisdom-Holman integrator), and close encounters and direct collisions (detected by the Visser algorithm) can be tracked accurately and efficiently. Such a combination is promising for statistical studies of subjects like the formation of exoplanetary systems, where often the computing power isn't there to perform many extremely high-accuracy simulations. In these cases an integration scheme incorporating both the Wisdom-Holman method and a method of detecting close encounters could be efficient enough to run a great many different initial conditions [4], while still being precise enough to capture the general structure of the system accurately.

The benefit of such a scheme depends critically on understanding the practical limitations of symplectic methods. While the Wisdom–Holman scheme is theoretically second-order accurate and remarkably stable for near-integrable systems, its performance in the presence of mean-motion resonances, step size resonances, and large time steps is less straightforward. Poorly chosen time steps can introduce numerical artifacts that may lead to spurious drift, breakdown of resonances, or artificial energy growth. Additionally, the choice of coordinate system, such as Jacobi or democratic heliocentric coordinates [5], influences how well the integrator performs.

This thesis aims to address the practical question: under what conditions can a Wisdom–Holman integrator deliver accurate and stable results even when using large time steps? Specifically, the following aspects will be investigated:

- The theoretical foundation of the Wisdom–Holman scheme, including Hamiltonian splitting, orbital averaging, and the symplectic nature of the integrator.
- The scaling behavior of numerical errors as a function of time step size Δt for both non-resonant and resonant systems.
- The presence and impact of step size resonances, and how they can artificially amplify numerical errors.
- A comparison between Jacobi coordinates and democratic heliocentric coordinates, to assess which approach offers better long-term stability and energy conservation.

All numerical experiments are performed using the open-source Rebound N-body integrator [6], which offers an efficient implementation of the WHfast algorithm [7], high-accuracy Kepler solvers, and flexible coordinate transformations.

2 Theory

2.1 The Classical Two-Body Problem

What distinguishes the Wisdom–Holman integration scheme from its close relative, the Leapfrog integrator, is its treatment of two-body interactions during the drift step. In particular, it replaces the standard drift with the exact solution to the two-body problem. To understand this step, we first review the classical two-body problem: the motion of two point masses interacting via Newtonian gravity. This includes its analytical solution and key mathematical tools such as the eccentric anomaly E and the so-called f- and g-functions,

2.1.1 Reduction to Relative Motion

Consider two point masses m_1 and m_2 interacting through Newton's law of gravitation. The acceleration of m_1 due to m_2 is given by

$$\ddot{\vec{r}}_1 = Gm_2 \frac{\vec{r}_2 - \vec{r}_1}{|\vec{r}_2 - \vec{r}_1|^3}, \tag{1}$$

and a similar equation holds for $\vec{r}_2$. Introducing the relative position vector $\vec{r} = \vec{r}_1 - \vec{r}_2$ and the total mass $M = m_1 + m_2$, we obtain the reduced equation of motion:

$$\ddot{\vec{r}} = -\mu \frac{\vec{r}}{r^3}, \qquad \mu = G(m_1 + m_2), \tag{2}$$

which describes the motion of a fictitious particle of reduced mass $m_r = \frac{m_1 m_2}{m_1 + m_2}$ in a central potential [1]. This equation implies conservation of energy and angular momentum. The latter ensures that the motion remains in a plane, which we can take as the xy-plane without loss of generality.

2.1.2 Solution as a Conic Section

The trajectory this equation describes is a conic section with one focus at the center of mass position. For bound systems (Energy $E < 0$), the solution is an *ellipse*. The position of the orbiting body as a function of time is most naturally described using six *orbital elements* instead of the six Cartesian components (three spatial components of both the position and momentum), which parameterize the shape and orientation of the orbit. These include the semi-major axis a (half the length of the longest diameter of the ellips), eccentricity e (the amount by which the orbit deviates from a circle), time of periapsis (closest point to the central body) passage τ, and orientation angles (inclination i, longitude of ascending node Ω, argument of periapsis ω)[8].

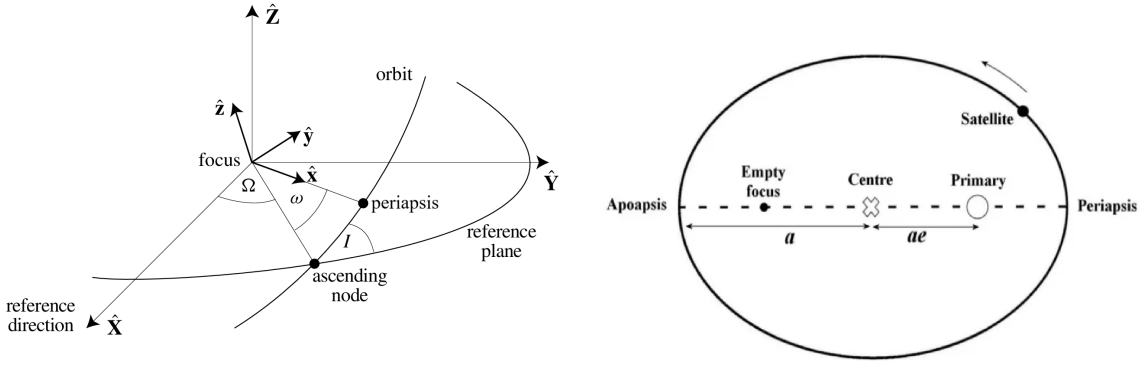

Figure 3: Illustration of orbital elements. Figure adapted from [1, 9].

To track the evolution of the position over time, we define the *mean anomaly* M. It's defined as [1]:

$$\mathsf{M} = \frac{2\pi}{\mathsf{T}}(t - \tau) \tag{3}$$

Here, t is time, and T is the period of the orbit, which can be calculated using [1]:

$$\mathsf{T}^2 = \frac{4\pi^2}{\mu} a^3 \tag{4}$$

The eccentric anomaly E is an angular parameter that indirectly gives the position on the ellipse, and is related to M by *Kepler's equation*[1]:

$$\mathsf{M} = \mathsf{E} - e \sin \mathsf{E} \tag{5}$$

This transcendental equation cannot be inverted analytically, but can be solved efficiently via iterative methods such as Newton-Raphson [10]. Once E is known, the Cartesian coordinates in the orbital plane can be computed via

$$x = a(\cos \mathsf{E} - e), \qquad y = a\sqrt{1 - e^2} \sin \mathsf{E} \tag{6}$$

which can then be rotated into the inertial frame using the orbital orientation angles.

2.1.3 Propagation via f and g Functions

The method shown in the previous subsection takes a lot of computation and extra steps that can be avoided. An alternative and advantageous method to propagate the motion of a body in a central potential is through the so-called f- and g-*functions*, which allow us to write the position and velocity at time t in terms of their values at an earlier time t_0 as:

$$\vec{r}(t) = f(t, t_0)\, \vec{r}_0 + g(t, t_0)\, \vec{v}_0, \tag{7}$$

$$\vec{v}(t) = \dot{f}(t, t_0)\,\vec{r}_0 + \dot{g}(t, t_0)\,\vec{v}_0. \tag{8}$$

These functions depend only on the time difference $\Delta t = t - t_0$, the gravitational parameter μ, and the initial orbital elements. They encapsulate the full solution to the two-body problem in terms of initial position and velocity, without explicitly referring to orbital elements [11].
To compute f and g, one typically proceeds by first solving a version of the Kepler equation for the eccentric anomaly or a related universal variable. For elliptic motion, the functions take the form:

$$f = 1 - \frac{a}{r_0}(1 - \cos \Delta \mathsf{E}), \tag{9}$$

$$g = \Delta t - \sqrt{\frac{a^3}{\mu}}(\Delta \mathsf{E} - \sin \Delta \mathsf{E}), \tag{10}$$

where $\Delta \mathsf{E} = \mathsf{E}(t) - \mathsf{E}(t_0)$. The derivatives $\dot{f}$ and $\dot{g}$ can be obtained from the time derivatives of these expressions.

2.2 Mean-Motion Resonances

Mean-motion resonances (MMRs) are a fundamental dynamical feature that can occur in multi-body gravitational systems, particularly in planetary systems. An MMR occurs when two orbiting bodies have orbital periods that are close to a ratio of small integers. In such configurations, the gravitational interactions between the bodies repeat periodically, resulting in long-term dynamical effects, such as phase locking and orbital protection. The theory behind this is quite complex and beyond the scope of this thesis; however, a brief overview of the essential concepts that will be used later is provided.

2.2.1 Definition and Basic Theory

Let n_1 and n_2 be the mean motions (average angular frequencies) of two orbiting bodies around a central mass:

$$n_i = \frac{2\pi}{\mathsf{T}_i}, \tag{11}$$

where T_i is the orbital period of the i-th body. The system is said to be near a *p:q mean-motion resonance* if

$$\frac{n_1}{n_2} \approx \frac{p}{q}, \tag{12}$$

for integers p and q. Typically, $p > q$ denotes an inner body orbiting faster than the outer. For example, in the well-known 3:2 resonance between Pluto and Neptune, Pluto completes two orbits for every three of Neptune [1].

2.2.2 Resonant Angles and Libration

Resonant angles are combinations of orbital elements that encapsulate the phase synchronization between the two bodies. For a $p+1$:p resonance (like the 3:2 resonance between Pluto and Neptune), two of those resonant angles take the form [12]:

$$\phi_1 = (p+1)\lambda_2 - p\lambda_1 - \varpi_1,$$

$$\phi_2 = (p+1)\lambda_2 - p\lambda_1 - \varpi_2, \tag{13}$$

where $\lambda_i = M_i + \varpi_i$ is the mean longitude, M_i is the mean anomaly, and $\varpi_i = \Omega + \omega$ is the longitude of periapsis of body i. ϕ_i is the angle between the position of the ith body at conjunction (when the two bodies line up) and the perihelion of that body's orbit.
The evolution of ϕ determines whether the system is truly in resonance. If ϕ circulates uniformly through all angles in $[0, 2\pi)$, the system is not resonant. If instead ϕ oscillates or *librates* around a fixed value (commonly 0 or π), the system is in resonance. This libration reflects a bounded phase relationship between the orbits, effectively locking the relative positions of the bodies in a repeating pattern.
For instance, for the Pluto-Neptune case:

$$\phi_{Pluto} = 3\lambda_{Pluto} - 2\lambda_{Neptune} - \varpi_{Pluto} \approx \pi, \tag{14}$$

This means that when the two are in conjunction (when they line up), Pluto is 180° away from its periapsis, so it is at its farthest point from the Sun. Because Neptune has a very circular orbit ($e \approx 0.01$), and Pluto quite an elliptic orbit ($e \approx 0.25$ [13], this means Pluto is always at its farthest point from Neptune's orbit when they line up (as illustrated in the figure below) meaning the two will never have an encounter even though their orbits cross. In fact, Pluto never gets closer than around $16AU$ to Neptune [14], meaning that Pluto's orbit is protected from significant changes that could occur if a close encounter with Neptune were possible.

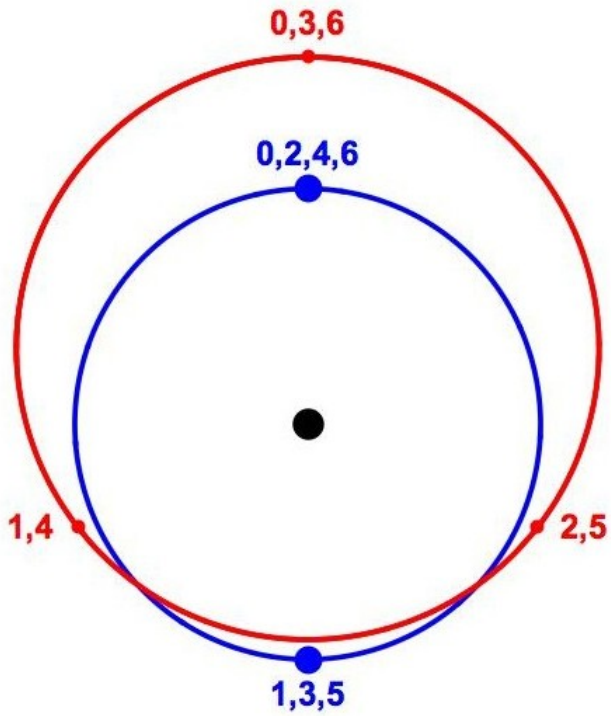

Figure 4: At the initial time, Neptune (blue) and Pluto (red) are in conjunction at the aphelion of Pluto. Numbers indicate their positions at intervals of half a Neptunean year, for a total of three Neptunean years. It's clear how the two will never have a close encounter. Figure and Caption adapted from [15].

This bounded behavior, which maintains resonance, arises from a restoring torque near the resonance. The resonant angle then behaves like the coordinate of a nonlinear oscillator, analogous to the motion of a pendulum, with its libration amplitude and frequency describing the width and timescale of the resonant interaction.

2.2.3 Libration Period

The libration period of the resonant angle, often denoted T_{lib}, is the timescale associated with the oscillation of the resonant angle around its mean point (it's also the period at which a lot of other orbital parameters like Pluto's orbital period oscillate). It is significantly longer than the individual orbital periods and characterizes the time required for the resonant angle to complete one full oscillation. The libration period depends sensitively on the proximity to exact commensurability, the masses of the bodies, and the eccentricities of the orbits. The libration period for the resonance between Pluto and Neptune is $\mathsf{T}_{\text{lib}} \approx 2 \cdot 10^4 yr$ [16]. The following figure shows this oscillation or orbital parameters.

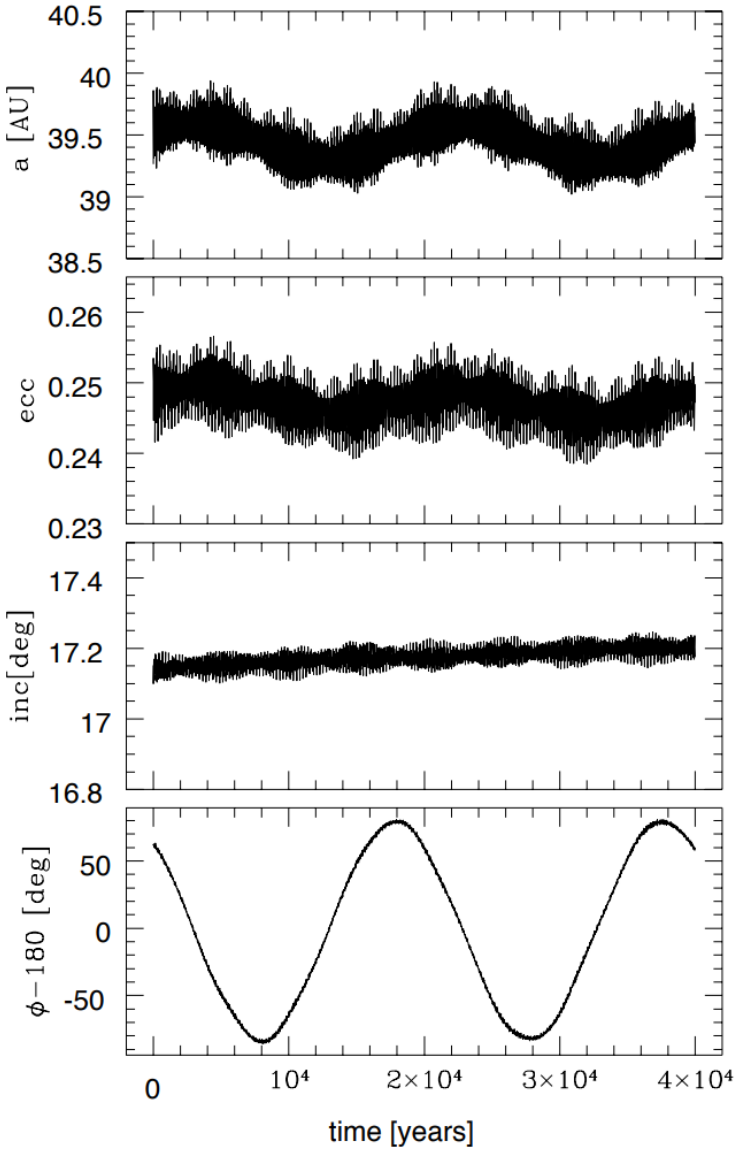

Figure 5: The variation of Pluto's orbital elements over 40,000 years: the semimajor axis, eccentricity, inclination are shown in the upper three panels. The bottom panel shows the libration of the resonance angle with a period of about 20,000 years. The 20,000 year periodic variations are evident in the semimajor axis and eccentricity, but not the inclination. The latter is only very weakly affected by Pluto's 3:2 mean motion resonance with Neptune. Figure and Caption reproduced from [16].

2.3 Center of Mass Motion

As will be seen later, the motion of the barycenter (center of mass) should be considered carefully. That is why the equations describing the motion of the barycenter of an n-body system are presented here. Firstly, the total mass M will be defined as:

$$M = \sum_{i=1}^{N} m_i. \tag{15}$$

Here m_i is the mass of the i^{th} body. Now the location of the barycenter can be written as:

$$\mathbf{R}_{\mathrm{CM}} = \frac{1}{M} \sum_{i=1}^{N} m_i \mathbf{r}_i, \tag{16}$$

$\mathbf{r}_i$ is the position vector of the i^{th} body. The velocity of the barycenter can be written as:

$$\mathbf{V}_{\mathrm{CM}} = \frac{1}{M} \sum_{i=1}^{N} m_i \mathbf{v}_i \tag{17}$$

$\mathbf{v}_i$ is the velocity vector of the i^{th} body. The total linear momentum of the system is then:

$$\mathbf{P}_{\mathrm{tot}} = \sum_{i=1}^{N} m_i \mathbf{v}_i = M \mathbf{V}_{\mathrm{CM}} \tag{18}$$

The acceleration of the barycenter is calculated using the following formula:

$$\ddot{\mathbf{R}}_{\mathrm{CM}} = \frac{1}{M} \sum_{i=1}^{N} \mathbf{F}_i = \frac{1}{M} \mathbf{F}_{\mathrm{ext}} \tag{19}$$

Here $\vec{F}_i$ is the total force experienced by the i^{th} body, and the last inequality follows from the fact that interaction forces between the bodies in the system always form pairs of equal size and opposite direction (Newton's third law), so the only remaining forces are external, which in the systems discussed in this paper are taken to be zero. In this case, an internal reference frame can always be chosen where the total linear momentum is zero.

2.4 N-body Problem

Now that the groundwork has been laid by defining and solving the 2-body problem and by presenting the equations describing the center of mass motion, we can move on to the N-body problem we set out to solve. In this subsection, the Hamiltonian of the system will be introduced, a way of splitting this Hamiltonian into a Kepler part and a perturbation part will be shown, and to give a clear example of this idea this will be fully worked out for a 3-body system.

2.4.1 The Hamiltonian of an N-body system

The Hamiltonian of a system is simply the sum of its potential and kinetic energy. The kinetic energy of the i^{th} body in the system is defined as $\mathcal{T}_i = \frac{\mathbf{p_i}^2}{2m_i}$. Every pair of bodies has an associated

potential energy of the Newtonian gravitational interaction between the two bodies, which is defined as $\mathcal{U}_{ij} = -\frac{Gm_i m_j}{|\vec{r_i} - \vec{r_j}|}$. This gives the following Hamiltonian for the entire system:

$$\mathcal{H}_{total} = \mathcal{T}_{total} + \mathcal{U}_{total} = \sum_{i=0}^{n} \frac{\mathbf{p_i}^2}{2m_i} + \sum_{i=0}^{n} \sum_{j=i+1}^{n} (-\frac{Gm_i m_j}{|\mathbf{r_i} - \mathbf{r_j}|}) \tag{20}$$

3 Numerical Integration

An analytical solution to the equations of motion is only available for the two-body problem as found in section 2.1. Once the number of interacting bodies exceeds two, $n > 2$, the system becomes nonlinear and generally unsolvable in closed form due to the emergence of chaotic dynamics and complex mutual interactions [1]. This makes numerical integration an essential tool for studying the evolution of multi-body systems, such as planetary systems, asteroid belts, or stellar clusters.
However, standard numerical methods often suffer from long-term energy drift, which can severely compromise the physical reliability of simulations over astronomical timescales. This is especially problematic in near-integrable systems, such as the Solar system, where small integration errors can accumulate and obscure genuine dynamical behavior. To address this, structure-preserving methods such as symplectic integrators have been developed, which are designed to conserve the Hamiltonian structure of the equations of motion [17].
The remainder of this section introduces the concept of symplectic integrators, the Leapfrog method, and then focuses on the Wisdom-Holman integrator. A few different coordinate systems for the Wisdom-Holman integrator will also be introduced, in particular the Jacobi and democratic heliocentric coordinates.

3.1 Symplectic Integrators

In numerical simulations of Hamiltonian systems, it is crucial not only to approximate trajectories accurately over short timescales, but also to preserve the system's qualitative behaviour over extended periods. Standard numerical methods, such as Runge-Kutta schemes, often introduce small energy errors that accumulate over time, leading to artificial energy drift. This drift can result in qualitatively incorrect dynamics, such as unphysical spiralling or escape of celestial bodies, which are not present in the actual physical system [17].
Symplectic integrators are a class of numerical methods designed explicitly for Hamiltonian systems. They preserve the symplectic structure of the continuous equations of motion, ensuring that specific geometric properties, like conserved phase space volume, are satisfied. While these integrators do not conserve energy exactly at each step, they confine energy errors to bounded, quasi-periodic oscillations over very long timescales. This makes them particularly well-suited for simulations in celestial mechanics, where integration timescales may span millions or billions of orbits [18].
A powerful insight underlying many symplectic methods is the idea of *Hamiltonian splitting*. Many physical Hamiltonians can be expressed as the sum of two simpler components:

$$\mathcal{H}(r, p) = \mathcal{A}(p) + \mathcal{B}(r) \tag{21}$$

where $\mathcal{A}(p)$ depends only on the momenta p and typically represents the kinetic energy, and $\mathcal{B}(r)$ depends only on the positions r and represents the potential energy. The Hamiltonian flows generated by $\mathcal{A}$ and $\mathcal{B}$ individually can often be solved exactly. In such cases, a symplectic integrator can be constructed by alternating between the exact solutions of these two subsystems.
This technique, known as *operator splitting*, allows for the construction of approximate solutions to the full system by composing simpler flows. For example, evolving first under $\mathcal{B}$ for a small timestep $\Delta t/2$, then under $\mathcal{A}$ for a complete step Δt, and again under $\mathcal{B}$ for $\Delta t/2$, yields a second-order accurate (third-order local truncation error) approximation to the full dynamics over time Δt, as in the end both parts of the Hamiltonian are each evolved over an entire time step. Crucially,

this composition remains symplectic, that is, it preserves the essential structure of the original Hamiltonian system [19].
The following notation is used for this numerical procedure:

$$E_{\mathcal{B}}(\tfrac{\Delta t}{2}) \circ E_{\mathcal{A}}(\Delta t) \circ E_{\mathcal{B}}(\tfrac{\Delta t}{2}), \tag{22}$$

where $E_{\mathcal{X}}(\Delta t)$ denotes evolution under Hamiltonian $\mathcal{X}$ for time Δt.

The Leapfrog Integrator. An example of perhaps the most well known symplectic integrator arising from operator splitting is the *Leapfrog method*, also known as the Störmer-Verlet or Velocity Verlet integrator. This method is particularly effective for systems where the Hamiltonian is separable into kinetic and potential energy components, so:

$$\mathcal{H}(r, p) = \mathcal{T}(p) + \mathcal{U}(r) \tag{23}$$

The Leapfrog integrator interleaves updates of positions and momenta as follows:

1. **Half-step momentum update (kick):**

$$p_{n+\frac{1}{2}} = p_n - \frac{\Delta t}{2} \nabla_r \mathcal{U}(r_n) \tag{24}$$

2. **Full-step position update (drift):**

$$r_{n+1} = r_n + \Delta t \nabla_p \mathcal{T}(p_{n+\frac{1}{2}}) \tag{25}$$

3. **Half-step momentum update (kick):**

$$p_{n+1} = p_{n+\frac{1}{2}} - \frac{\Delta t}{2} \nabla_r \mathcal{U}(r_{n+1}) \tag{26}$$

So, in proper notation, leapfrog in its kick-drift-kick is:

$$E_{\text{kick}}(\tfrac{\Delta t}{2}) \circ E_{\text{drift}}(\Delta t) \circ E_{\text{kick}}(\tfrac{\Delta t}{2}), \tag{27}$$

This "kick-drift-kick" sequence is both time-reversible and symplectic. Its
second-order accuracy arises from the symmetric composition of the exact flows of $\mathcal{T}$ and $\mathcal{U}$. Specifically, the local truncation error per step is of order $\mathcal{O}(\Delta t^3)$. The global error then scales with the truncation error times the amount of steps $\mathsf{N} = \frac{T}{\Delta t}$ (Where T is the total runtime), So the global error is of order $\mathcal{O}(\Delta t^2)$ making leapfrog a second order integrator [17]. The Leapfrog integrator's symplectic nature ensures that it preserves the qualitative features of Hamiltonian dynamics over long timescales. Unlike non-symplectic methods, which may exhibit secular energy drift, the Leapfrog method confines energy errors to bounded oscillations, maintaining the system's stability and fidelity in long-term simulations [18].

3.2 Wisdom-Holman Schemes

3.2.1 Splitting of the Hamiltonian

There are many ways to split the Hamiltonian of an N-body system as given in formula (20), but to illustrate the idea, we will perform a simple split. As we are interested in systems with a perturbation that is small compared to the analytical (Kepler) part, the assumption is made that the system contains a particle with a significantly larger mass than the others (e.g., a star). We choose an ordering such that this particle has index 0. We can now write the Hamiltonian (20) as follows:

$$\mathcal{H}_{\text{total}} = \sum_{i=1}^{n}(\frac{\mathbf{p_i}^2}{2m_i} - \frac{Gm_im_j}{|\mathbf{r_i} - \mathbf{r_0}|}) + \sum_{i=1}^{n}\sum_{j=i+1}^{n}(-\frac{Gm_im_j}{|\mathbf{r_i} - \mathbf{r_j}|}) + \frac{\mathbf{p_0}^2}{2m_0} \tag{28}$$

and because the Hamiltonian of a 2-body system with a fixed sun is:

$$\mathcal{H}_{\text{kep}_i} = \frac{\mathbf{p_i}^2}{2m_i} - \frac{GM_0m_i}{|\mathbf{r_i} - \mathbf{r_0}|} \tag{29}$$

It is clear that now the total Hamiltonian (28) can be written as:

$$\mathcal{H}_{\text{total}} = \sum_{i=1}^{n}\mathcal{H}_{\text{kep}_i} + \sum_{i=1}^{n}\sum_{j=i+1}^{n}(-\frac{Gm_im_j}{|\mathbf{r_i} - \mathbf{r_j}|}) + \frac{\mathbf{p_0}^2}{2m_0} = \mathcal{H}_{\text{kep}} + \mathcal{H}_{\text{pert}} \tag{30}$$

where the Kepler Hamiltonian $\mathcal{H}_{\text{kep}} = \sum_{i=1}^{n}\mathcal{H}_{\text{kep}_i}$
and the perturbation Hamiltonian $\mathcal{H}_{\text{pert}} = \sum_{i=1}^{n}\sum_{j=i+1}^{n}(-\frac{Gm_im_j}{|\mathbf{r_i}-\mathbf{r_j}|}) + \frac{\mathbf{p_0}^2}{2m_0}$.
As long as the bodies don't get too close to each other, and because the kinetic energy of the heavy particle will always be much lower than that of the other bodies, the perturbation term is expected to be much smaller than the analytical Kepler term. This is the key insight behind Wisdom-Holman integration schemes. These involve splitting the Hamiltonian of the total system in such a way that it has one (dominant) part with only analytical Kepler solutions, and a much smaller perturbation term. However, a subtle issue arises because of the $\frac{\mathbf{p_0}^2}{2m_0}$ term in the perturbation Hamiltonian. In the Kepler step (analogous to the drift step in the leapfrog integrator), the position of the central mass is assumed to be fixed so that each particle's Kepler orbit can be evolved independently. However, this means that the central mass does not actually move during the Kepler evolution, which in turn means that the evolution of $\mathbf{p}_0$ isn't captured in the Kepler step. So, when we try to evolve the perturbation Hamiltonian, we are left with the kinetic energy term $\frac{\mathbf{p_0}^2}{2m_0}$ by itself, but no remaining force terms that would correctly describe how $\mathbf{p}_0$ should evolve. This means the central body's momentum is assumed constant in the perturbation step, which leads to a constant drift in the central body (when $\mathbf{p}_0 \neq 0$), which is, of course, unphysical. When $\frac{\mathbf{p_0}^2}{2m_0}$ is taken to be approximately 0 (e.g. a fixed sun) then instead of $\mathcal{H}_{\text{pert}}$ we have the purely interaction-based Hamiltonian $\mathcal{H}_{\text{int}} = \sum_{i=1}^{n}\sum_{j=i+1}^{n}(-\frac{Gm_im_j}{|\mathbf{r_i}-\mathbf{r_j}|})$ which can be solved analytically. So we get the following integration scheme:

$$E_{\text{int}}(\tfrac{\Delta t}{2}) \circ E_{\text{kep}}(\Delta t) \circ E_{\text{int}}(\tfrac{\Delta t}{2}), \tag{31}$$

This is the form of most Wisdom-Holman integration schemes; however, we had to make an approximation here to obtain an analytic solution to $\mathcal{H}_{\text{pert}}$ that makes physical sense. However, to ensure

integration schemes converge to the real solution, we must avoid approximations in the Hamiltonian, such as these. Therefore, two different coordinate transformations will now be introduced, which yield splits in the Hamiltonian such that each part is analytically solvable, meaning these parts can be combined into a symplectic integrator.

3.2.2 Jacobi Coordinates

The most common splitting of the Hamiltonian for use in the Wisdom-Holman integrator is done by using Jacobi coordinates, which are defined as follows [5].
Consider a system of N bodies with masses $m_0, m_1, \ldots, m_{N-1}$ and positions $\mathbf{r}_0, \mathbf{r}_1, \ldots, \mathbf{r}_{N-1}$ in an inertial frame. Without loss of generality, let m_0 denote the central mass (e.g., the Sun).
Let N point masses have positions $\mathbf{r}_i \in \mathbb{R}^3$, velocities $\dot{\mathbf{r}}_i$, masses m_i, and canonical momenta $\mathbf{p}_i = m_i\dot{\mathbf{r}}_i$, for $i = 0, 1, \ldots, N-1$. This ordering isn't arbitrary however, as for the Jacobi coordinates it's crucial that the ordering goes from the inside of the system (the central mass) to the outside (e.g. ideally the orbit of the $(i-1)^{th}$ body lies fully within the orbit of the i^{th} body).

Center of Mass To define the Jacobi Coordinates, first, different centers of mass need to be defined:

$$M_i = \sum_{j=0}^{i} m_j, \qquad \mathbf{R}_i = \frac{1}{M_i}\sum_{j=0}^{i} m_j\mathbf{r}_j. \tag{32}$$

This equates to $\mathbf{R}_i$ being the center of mass of all bodies up to and including index i, note that $M_{\mathrm{CM}} = M_{N-1}$ and $\mathbf{R}_{\mathrm{CM}} = \mathbf{R}_{N-1}$.

Jacobi Positions The Jacobi Positions $\tilde{\mathbf{r}}_i$ themselves are then defined as follows:

$$\tilde{\mathbf{r}}_0 = \mathbf{R}_{\mathrm{CM}}, \qquad \tilde{\mathbf{r}}_i = \mathbf{r}_i - \mathbf{R}_{i-1}, \quad \text{for } i = 1, \ldots, N-1. \tag{33}$$

Which means $\tilde{\mathbf{r}}_0$ is the center of mass of the entire system and $\tilde{\mathbf{r}}_i$ for $i \geq 1$ is the position of the i^{th} body relative to the center of mass of all the bodies with index less than i.

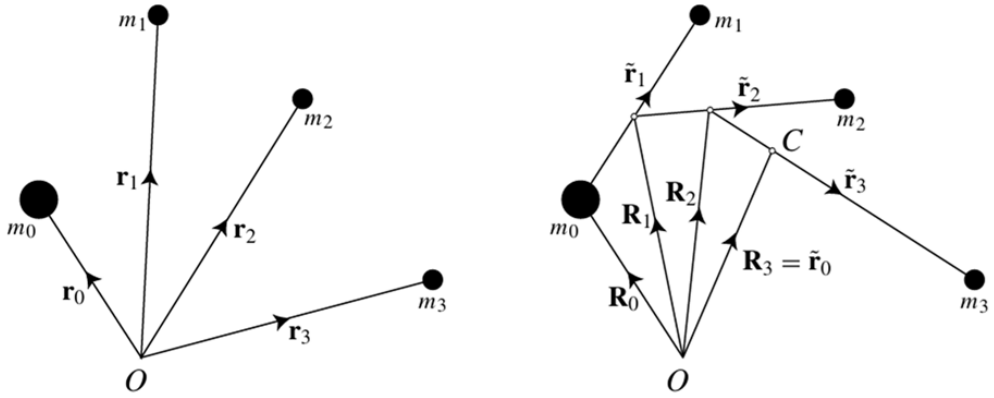

Figure 6: On the left, Cartesian coordinates, and on the right, the Jacobi coordinates. $\tilde{\mathbf{r}}_i$ is now defined as the position of the i^{th} body relative to the center of mass of all the bodies with index less than i $\mathbf{R}_{i-1}$, except for $\tilde{\mathbf{r}}_0$ which is the center of mass of the entire system. Figure reproduced from [1]

Reduced Masses These are defined as:

$$\mu_i = \frac{M_{i-1} \cdot m_i}{M_i}, \quad \text{for } i \geq 1. \tag{34}$$

Jacobi Momenta The canonical Jacobi Momenta can be obtained using a generating function [5], but maybe a more intuitive way to do this is using Lagrangian mechanics [20]. To derive the canonical momenta, we begin with the total kinetic energy of the system written in Jacobi coordinates. This can be rewritten in the following way [1]:

$$\mathcal{T}_{\text{total}} = \frac{1}{2} M \dot{\tilde{\mathbf{r}}}_0^2 + \sum_{i=1}^{N-1} \frac{1}{2} \mu_i \dot{\tilde{\mathbf{r}}}_i^2. \tag{35}$$

The Lagrangian of the system is:

$$\mathcal{L}(\tilde{\mathbf{r}}_0, \ldots, \tilde{\mathbf{r}}_{N-1}, \dot{\tilde{\mathbf{r}}}_0, \ldots, \dot{\tilde{\mathbf{r}}}_{N-1}) = \mathcal{T}_{\text{total}} - \mathcal{U}_{\text{total}}, \tag{36}$$

and canonical momenta $\tilde{\mathbf{p}}_i$ conjugate to the Jacobi coordinates $\tilde{\mathbf{r}}_i$ are given by:

$$\tilde{\mathbf{p}}_i = \frac{\partial \mathcal{L}}{\partial \dot{\tilde{\mathbf{r}}}_i}. \tag{37}$$

Note that the potential energy $\mathcal{U}_{\text{total}}$ depends on the original coordinates $\mathbf{r}_i$, which are implicitly functions of the Jacobi positions $\tilde{\mathbf{r}}_i$. However, since we are taking derivatives with respect to velocities to obtain the momenta, only the kinetic part contributes.

Case $i = 0$: We recall that $\tilde{\mathbf{r}}_0 = \mathbf{R}_{\text{CM}}$, so:

$$\tilde{\mathbf{p}}_0 = \frac{\partial \mathcal{L}}{\partial \dot{\tilde{\mathbf{r}}}_0} = \frac{\partial}{\partial \dot{\tilde{\mathbf{r}}}_0} \left(\frac{1}{2} M_{\text{CM}} \dot{\tilde{\mathbf{r}}}_0^2 \right) = M_{\text{CM}} \dot{\tilde{\mathbf{r}}}_0 = \mathbf{P}_{\text{CM}}. \tag{38}$$

So it's just the momentum of the center of mass.

Case $i \geq 1$: For the other bodies, we compute:

$$\tilde{\mathbf{p}}_i = \frac{\partial \mathcal{L}}{\partial \dot{\tilde{\mathbf{r}}}_i} = \frac{\partial}{\partial \dot{\tilde{\mathbf{r}}}_i} \left(\sum_{j=1}^{N-1} \frac{1}{2} \mu_j \dot{\tilde{\mathbf{r}}}_j^2 \right) = \mu_i \dot{\tilde{\mathbf{r}}}_i. \tag{39}$$

Recalling the definition of $\tilde{\mathbf{r}}_i = \mathbf{r}_i - \mathbf{R}_{i-1}$, and using the velocity form:

$$\dot{\tilde{\mathbf{r}}}_i = \dot{\mathbf{r}}_i - \dot{\mathbf{R}}_{i-1}, \tag{40}$$

we finally obtain:

$$\tilde{\mathbf{p}}_i = \mu_i (\dot{\mathbf{r}}_i - \dot{\mathbf{R}}_{i-1}), \tag{41}$$

Total Kinetic Energy Can now be written as:

$$\mathcal{T}_{\text{total}} = \sum_{i=1}^{N-1} \frac{\tilde{\mathbf{p}}_i^2}{2\mu_i} + \frac{\tilde{\mathbf{p}}_0^2}{2M}, \quad \text{where } M = M_{N-1} = \sum_{i=0}^{N-1} m_i \tag{42}$$

In the center-of-mass frame ($\tilde{\mathbf{p}}_0 = 0$), this becomes:

$$\mathcal{T}_{\text{total}} = \sum_{i=1}^{N-1} \frac{\tilde{\mathbf{p}}_i^2}{2\mu_i}. \tag{43}$$

Potential Energy

$$\mathcal{U}_{\text{total}} = -G \sum_{0 \leq i < j < N} \frac{m_i m_j}{|\mathbf{r}_i - \mathbf{r}_j|}. \tag{44}$$

Total Hamiltonian

$$\mathcal{H}_{\text{total}} = \mathcal{T}_{\text{total}} + \mathcal{U}_{\text{total}} = \sum_{i=1}^{N-1} \frac{\tilde{\mathbf{p}}_i^2}{2\mu_i} - G \sum_{0 \leq i < j < N} \frac{m_i m_j}{|\mathbf{r}_i - \mathbf{r}_j|} \tag{45}$$

Wisdom-Holman Splitting We now decompose the Hamiltonian as:

$$\mathcal{H}_{\text{total}} = \mathcal{H}_{\text{kep}} + \mathcal{H}_{\text{int}}, \tag{46}$$

where:

Keplerian Part ($\mathcal{H}_{\text{kep}}$) This part assumes each body orbits the center of mass of the bodies with an index lower than its own (which is why it physically only makes sense if the bodies are ordered from the inside of the system outward):

$$\mathcal{H}_{\text{kep}} = \sum_{i=1}^{N-1} \left(\frac{\tilde{\mathbf{p}}_i^2}{2\mu_i} - G\frac{M_{i-1}m_i}{|\tilde{\mathbf{r}}_i|} \right). \tag{47}$$

Each term is a two-body Kepler problem in Jacobi coordinates.

Interaction Part ($\mathcal{H}_{\text{int}}$) This part contains the remainder of the full potential, after subtracting the potentials used in the Keplerian part:

$$\begin{aligned} \mathcal{H}_{\text{int}} &= \mathcal{U}_{\text{total}} - \sum_{i=1}^{N-1} \left(-G\frac{M_{i-1}m_i}{|\tilde{\mathbf{r}}_i|} \right). \\ &= -G \sum_{0 \le i < j < N} \frac{m_i m_j}{|\mathbf{r}_i - \mathbf{r}_j|} + G \sum_{i=1}^{N-1} \frac{M_{i-1}m_i}{|\tilde{\mathbf{r}}_i|}. \end{aligned} \tag{48}$$

Both these Hamiltonians lead to equations that can be analytically solved, which means we can construct the following symplectic integration scheme:

$$E_{\text{int}}(\tfrac{\Delta t}{2}) \circ E_{\text{kep}}(\Delta t) \circ E_{\text{int}}(\tfrac{\Delta t}{2}), \tag{49}$$

which indeed has the same form as equation 31.

3.2.3 Jacobi Coordinates for $N = 3$

We now specify the general Jacobi coordinate formulation to the case of three particles with masses m_0, m_1, m_2, and positions $\mathbf{r}_0, \mathbf{r}_1, \mathbf{r}_2$. This is intended to provide a clearer understanding of what is actually happening.

Center of Masses We define the cumulative masses and corresponding centers of mass:

$$\begin{aligned} M_0 &= m_0, & \mathbf{R}_0 &= \mathbf{r}_0, \\ M_1 &= m_0 + m_1, & \mathbf{R}_1 &= \frac{m_0\mathbf{r}_0 + m_1\mathbf{r}_1}{m_0 + m_1}, \\ M_2 &= m_0 + m_1 + m_2, & \mathbf{R}_2 &= \frac{m_0\mathbf{r}_0 + m_1\mathbf{r}_1 + m_2\mathbf{r}_2}{m_0 + m_1 + m_2}. \end{aligned}$$

Jacobi Positions The Jacobi positions $\tilde{\mathbf{r}}_i$ are then:

$$\begin{aligned} \tilde{\mathbf{r}}_0 &= \mathbf{R}_2, \\ \tilde{\mathbf{r}}_1 &= \mathbf{r}_1 - \mathbf{r}_0, \\ \tilde{\mathbf{r}}_2 &= \mathbf{r}_2 - \mathbf{R}_1 = \mathbf{r}_2 - \frac{m_0\mathbf{r}_0 + m_1\mathbf{r}_1}{m_0 + m_1}. \end{aligned}$$

Reduced Masses The corresponding reduced masses are:

$$\mu_1 = \frac{m_0 m_1}{m_0 + m_1},$$
$$\mu_2 = \frac{(m_0 + m_1) m_2}{m_0 + m_1 + m_2}.$$

Momenta The Jacobi canonical momenta $\tilde{\mathbf{p}}_i$ are:

$$\begin{aligned}
\tilde{\mathbf{p}}_0 &= m_0 \dot{\mathbf{r}}_0 + m_1 \dot{\mathbf{r}}_1 + m_2 \dot{\mathbf{r}}_2, \\
\tilde{\mathbf{p}}_1 &= \mu_1 (\dot{\mathbf{r}}_1 - \dot{\mathbf{r}}_0), \\
\tilde{\mathbf{p}}_2 &= \mu_2 \left(\dot{\mathbf{r}}_2 - \frac{m_0 \dot{\mathbf{r}}_0 + m_1 \dot{\mathbf{r}}_1}{m_0 + m_1} \right),
\end{aligned}$$

Kinetic Energy The total kinetic energy becomes:

$$\mathcal{T}_{\text{total}} = \frac{\tilde{\mathbf{p}}_1^2}{2\mu_1} + \frac{\tilde{\mathbf{p}}_2^2}{2\mu_2} + \frac{\tilde{\mathbf{p}}_0^2}{2M_2}.$$

In the center-of-mass frame $\tilde{\mathbf{p}}_0 = 0$, this simplifies to:

$$\mathcal{T}_{\text{total}} = \frac{\tilde{\mathbf{p}}_1^2}{2\mu_1} + \frac{\tilde{\mathbf{p}}_2^2}{2\mu_2}.$$

Potential Energy The gravitational potential energy remains in Cartesian coordinates (why will become clear later):

$$\mathcal{U}_{\text{total}} = -G \left(\frac{m_0 m_1}{|\mathbf{r}_0 - \mathbf{r}_1|} + \frac{m_0 m_2}{|\mathbf{r}_0 - \mathbf{r}_2|} + \frac{m_1 m_2}{|\mathbf{r}_1 - \mathbf{r}_2|} \right).$$

Total Hamiltonian

$$\mathcal{H}_{\text{total}} = \mathcal{T}_{\text{total}} + \mathcal{U}_{\text{total}} = \frac{\tilde{\mathbf{p}}_1^2}{2\mu_1} + \frac{\tilde{\mathbf{p}}_2^2}{2\mu_2} - G \left(\frac{m_0 m_1}{|\mathbf{r}_0 - \mathbf{r}_1|} + \frac{m_0 m_2}{|\mathbf{r}_0 - \mathbf{r}_2|} + \frac{m_1 m_2}{|\mathbf{r}_1 - \mathbf{r}_2|} \right).$$

Wisdom-Holman Splitting We now split the Hamiltonian as:

$$\mathcal{H}_{\text{total}} = \mathcal{H}_{\text{kep}} + \mathcal{H}_{\text{int}},$$

where the Keplerian part is:

$$\mathcal{H}_{\text{kep}} = \frac{\tilde{\mathbf{p}}_1^2}{2\mu_1} - G\frac{m_0 m_1}{|\tilde{\mathbf{r}}_1|} + \frac{\tilde{\mathbf{p}}_2^2}{2\mu_2} - G\frac{(m_0 + m_1) m_2}{|\tilde{\mathbf{r}}_2|},$$

and the interaction part becomes:

$$\mathcal{H}_{\text{int}} = \mathcal{U}_{\text{total}} - \left(-G\frac{m_0 m_1}{|\tilde{\mathbf{r}}_1|} - G\frac{(m_0 + m_1) m_2}{|\tilde{\mathbf{r}}_2|} \right),$$

$$= -G\left(\frac{m_0 m_2}{|\mathbf{r}_0 - \mathbf{r}_2|} + \frac{m_1 m_2}{|\mathbf{r}_1 - \mathbf{r}_2|} - \frac{(m_0+m_1)^2 m_2}{|(m_0+m_1)\mathbf{r}_2 - m_0\mathbf{r}_0 - m_1\mathbf{r}_1|}\right).$$

The reason the interaction Hamiltonian is expressed in Cartesian coordinates instead of Jacobi coordinates (and also why we did this for $\mathcal{U}_{\text{total}}$) is that the interaction part leads to a kick to the particles, which is computationally much easier in Cartesian coordinates. Any data collection at each time step is generally desired in Cartesian coordinates as well. The usual approach is to convert to Jacobi coordinates only for the Kepler step and then convert back to Cartesian coordinates for the kicks.

3.2.4 Democratic Heliocentric Coordinates

An alternative to the Jacobi coordinate system for symplectic integration is the use of *democratic heliocentric coordinates*, as developed by [5]. These coordinates treat all planets on equal footing, while still using the heliocentric frame for positions and the barycentric frame for momenta.

Positions and Momenta Let the system consist of N particles with masses $m_0, m_1, \ldots, m_{N-1}$, positions $\mathbf{r}_i \in \mathbb{R}^3$, and canonical momenta $\mathbf{p}_i = m_i \dot{\mathbf{r}}_i$, where $i = 0$ refers to the central mass (e.g., the Sun). We define a new set of canonical coordinates $(\mathbf{Q}_i, \mathbf{P}_i)$ as follows:

$$\mathbf{Q}_0 = \mathbf{R}_{\text{CM}} = \frac{1}{M}\sum_{j=0}^{N-1} m_j \mathbf{r}_j, \qquad \text{(center of mass position, for } i = 0)$$

$$\mathbf{Q}_i = \mathbf{r}_i - \mathbf{r}_0, \qquad \text{(heliocentric positions, for } i \geq 1) \tag{50}$$

with total mass $M = \sum_{j=0}^{N-1} m_j$. The corresponding canonical momenta $\mathbf{P}_i$ are derived again from the Lagrangian:

$$\mathcal{L} = \sum_{i=0}^{N-1} \frac{1}{2} m_i \dot{\mathbf{r}}_i^2 - \mathcal{U}(\mathbf{Q}_1, \ldots, \mathbf{Q}_{N-1}), \tag{51}$$

which simplifies to:

$$\mathcal{L} = \frac{1}{2} M \dot{\mathbf{Q}}_0^2 + \sum_{i=1}^{N-1} \frac{1}{2} m_i \left(\dot{\mathbf{Q}}_i - \sum_{j=1}^{N-1} \frac{m_j}{M} \dot{\mathbf{Q}}_j\right)^2 - \mathcal{U}. \tag{52}$$

From this Lagrangian, we derive the canonical momenta:

$$\mathbf{P}_0 = \frac{\partial \mathcal{L}}{\partial \dot{\mathbf{Q}}_0} = M\dot{\mathbf{Q}}_0 = \mathbf{P}_{CM} = \sum_{i=0}^{N-1} \mathbf{p}_i, \tag{53}$$

$$\mathbf{P}_i = \frac{\partial \mathcal{L}}{\partial \dot{\mathbf{Q}}_i} = m_i \left(\dot{\mathbf{Q}}_i - \sum_{j=1}^{N-1} \frac{m_j}{M} \dot{\mathbf{Q}}_j\right) = \mathbf{p}_i - \frac{m_i}{M} \sum_{j=0}^{N-1} \mathbf{p}_j \quad \text{for } i \geq 1. \tag{54}$$

So for $i \geq 1$ the positions are heliocentric (relative to the central mass) and momenta are barycentric (relative to the center of mass).

Hamiltonian In these coordinates, the total Hamiltonian becomes:

$$\mathcal{H}(\mathbf{Q}_i, \mathbf{P}_i) = \sum_{i=1}^{N-1} \left(\frac{\mathbf{P}_i^2}{2m_i} - G\frac{m_0 m_i}{|\mathbf{Q}_i|} \right) + \frac{1}{2m_0} \left(\sum_{i=1}^{N-1} \mathbf{P}_i \right)^2 - G \sum_{1 \le i < j < N} \frac{m_i m_j}{|\mathbf{Q}_i - \mathbf{Q}_j|}. \tag{55}$$

This Hamiltonian is then naturally split into three parts:

$$\mathcal{H}_{\text{Kep}} = \sum_{i=1}^{N-1} \left(\frac{\mathbf{P}_i^2}{2m_i} - G\frac{m_0 m_i}{|\mathbf{Q}_i|} \right), \tag{56}$$

$$\mathcal{H}_{\odot} = \frac{1}{2m_0} \left(\sum_{i=1}^{N-1} \mathbf{P}_i \right)^2, \tag{57}$$

$$\mathcal{H}_{\text{int}} = -G \sum_{1 \le i < j < N} \frac{m_i m_j}{|\mathbf{Q}_i - \mathbf{Q}_j|} = -G \sum_{1 \le i < j < N} \frac{m_i m_j}{|\mathbf{r}_i - \mathbf{r}_j|}. \tag{58}$$

Wisdom-Holman Splitting (Democratic) The resulting second-order symplectic integrator evolves the system as:

$$E_{\odot}(\tfrac{\Delta t}{2}) \circ E_{\text{int}}(\tfrac{\Delta t}{2}) \circ E_{\text{Kep}}(\Delta t) \circ E_{\text{int}}(\tfrac{\Delta t}{2}) \circ E_{\odot}(\tfrac{\Delta t}{2}), \tag{59}$$

- $E_{\text{Kep}}(h)$ integrates the two-body Kepler problems of planets 1 and 2 around the Sun.
- $E_{\text{int}}(h)$ applies the mutual gravitational kick between planet 1 and planet 2.
- $E_{\odot}(h)$ corrects for the indirect acceleration due to the Sun's recoil.

This formulation ensures that all planetary bodies are treated equally in the Keplerian drift step, all revolving around the same point, so the ordering of the bodies doesn't matter, unlike when using Jacobi coordinates. However, the barycentric momenta are used in the Kepler step instead of the actual heliocentric momenta. As a result, the velocities used in the Keplerian evolution do not correspond to the physical velocities relative to the central body. This means that for a two-body system, this solution isn't exact for anything but the limit of $\Delta t \to 0$ (using Jacobi coordinates, it exact for the two-body system, no matter the size of the time step).

3.2.5 Democratic Heliocentric Coordinates for $N = 3$

We now explicitly work out the democratic heliocentric Hamiltonian for a system of three bodies: the Sun ($i = 0$) and two planets ($i = 1, 2$). The positions $\mathbf{Q}_1, \mathbf{Q}_2$ are heliocentric, and the momenta $\mathbf{P}_1, \mathbf{P}_2$ are barycentric.

Positions:

$$\mathbf{Q}_1 = \mathbf{r}_1 - \mathbf{r}_0,$$
$$\mathbf{Q}_2 = \mathbf{r}_2 - \mathbf{r}_0.$$

Momenta: Let the total momentum be $\mathbf{P}_0 = \mathbf{p}_0+\mathbf{p}_1+\mathbf{p}_2$, and the total mass $M = m_0+m_1+m_2$. Then:

$$\mathbf{P}_1 = \mathbf{p}_1 - \frac{m_1}{M}\mathbf{P}_0,$$
$$\mathbf{P}_2 = \mathbf{p}_2 - \frac{m_2}{M}\mathbf{P}_0.$$

the center of mass position and total momentum are:

$$\mathbf{Q}_0 = \frac{1}{M}(m_0\mathbf{r}_0 + m_1\mathbf{r}_1 + m_2\mathbf{r}_2),$$
$$\mathbf{P}_0 = \mathbf{p}_0 + \mathbf{p}_1 + \mathbf{p}_2.$$

Hamiltonian Terms The total Hamiltonian is written as:

$$\mathcal{H}(\mathbf{Q}_1, \mathbf{Q}_2, \mathbf{P}_1, \mathbf{P}_2) = \mathcal{H}_{\text{Kep}} + \mathcal{H}_{\odot} + \mathcal{H}_{\text{int}},$$

with:

Keplerian term:

$$\mathcal{H}_{\text{Kep}} = \frac{\mathbf{P}_1^2}{2m_1} - G\frac{m_0m_1}{|\mathbf{Q}_1|} + \frac{\mathbf{P}_2^2}{2m_2} - G\frac{m_0m_2}{|\mathbf{Q}_2|}.$$

Sun correction term:

$$\mathcal{H}_{\odot} = \frac{1}{2m_0}\left(\mathbf{P}_1 + \mathbf{P}_2\right)^2.$$

Interaction term:

$$\mathcal{H}_{\text{int}} = -G\frac{m_1m_2}{|\mathbf{r}_1 - \mathbf{r}_2|} = -G\frac{m_1m_2}{|\mathbf{Q}_1 - \mathbf{Q}_2|}.$$

4 Large Time Steps Δt

To make an integration scheme as efficient as possible, it is desirable to choose a time step Δt that is as large as possible, but of course, increasing the time step typically increases the numerical error. Surprisingly, there are good reasons to expect that Wisdom–Holman integrators can still achieve accurate results even when Δt is comparable to, or larger than, the shortest orbital period in the system. This idea can be motivated by the concept of orbital averaging. Celestial mechanicians used orbital averaging before the advent of numerical N-body simulations to estimate long-term perturbative effects. To illustrate this, consider a three-body system: two planets orbiting a central star. Suppose we want to find the long-term effect of planet 2 on the orbit of planet 1. While this effect cannot be solved exactly in general, it can be approximated by spreading the mass of planet 2 continuously along its orbit. The resulting mass distribution has a density inversely proportional to the planet's orbital speed; regions where the planet moves slowly contribute more mass because the planet spends more time there. This smears out short-term fluctuations, allowing the long-term perturbation to be solved analytically [1].

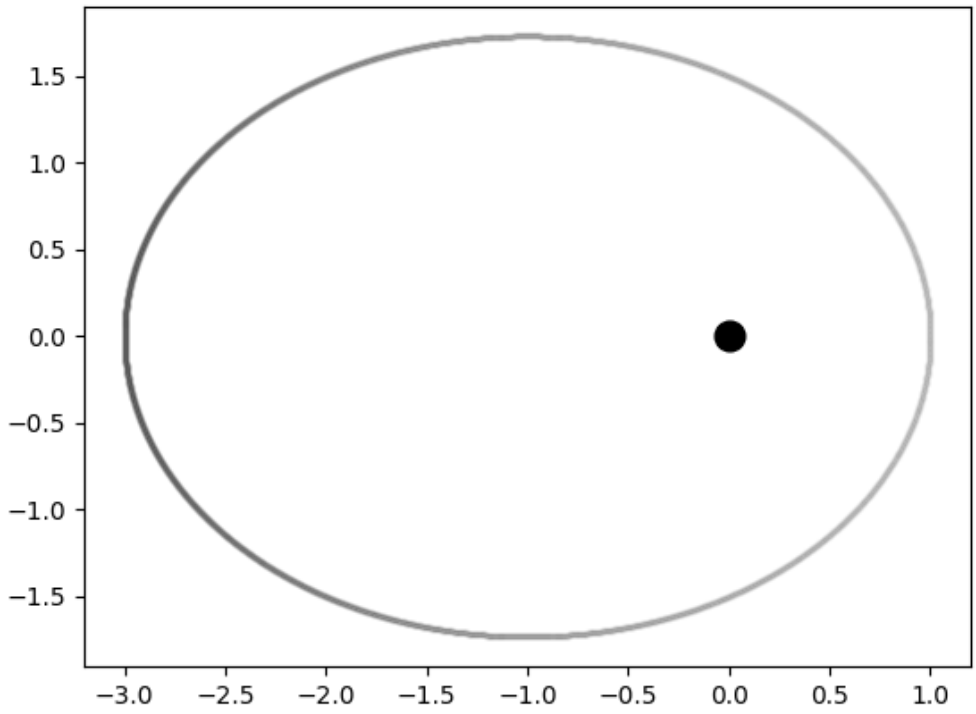

Figure 7: Illustration of orbital averaging: a body's mass is spread along its orbit with density inversely proportional to its orbital speed. This represents the time-averaged gravitational influence on another body.

In numerical integration, the idea is similar. When many small time steps are taken, the sampled positions of an orbiting body over time will naturally approximate this averaged mass distribution (see Fig. 8). In this sense, the numerical solution mimics the orbital averaging method, but with the advantage that it tracks the exact positions of the bodies at each step, so phenomena like mean-motion resonances, which depend on the precise relative positions of the bodies, are preserved. Orbital averaging alone cannot capture such effects.

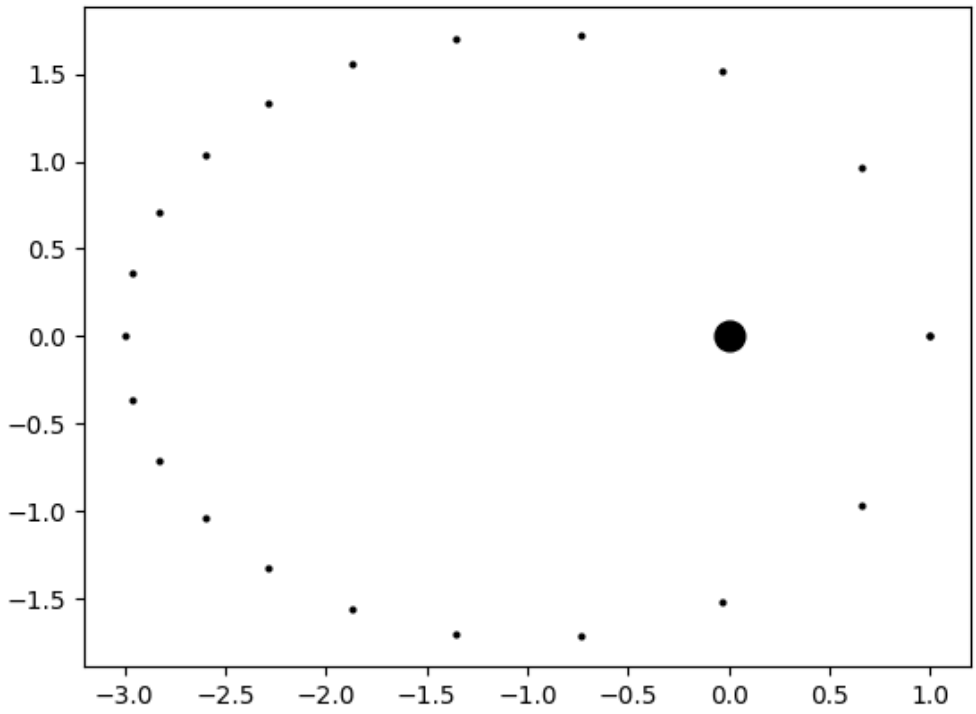

Figure 8: Positions of a body sampled at regular time intervals. The distribution of points approximates the orbital-averaged mass distribution shown in Figure 7.

The key insight for the Wisdom–Holman integrator is that it splits the system's Hamiltonian into two parts: the Keplerian motion, which is integrated exactly, and the smaller perturbative interactions, which are handled numerically. Because the drift step exactly follows each body's unperturbed Kepler orbit, the positions over a great many time steps still end up approximating the orbital-averaged mass distribution. So over many steps, the effect of the perturbations averages out in a way that is physically consistent with orbital averaging, while still preserving important dynamical features like resonances.
Of course, this picture breaks down if bodies experience close encounters, where the perturbative assumption no longer holds. But as long as interactions remain weak, this explains why Wisdom–Holman integrators can remain accurate even with time steps larger than the shortest orbital period.

5 The Rebound Package

All simulations in this thesis were performed using the Rebound package [6], an open-source N-body integrator written in C which can be imported into Python as a library. It's because of the significance to this thesis that first, this package will be properly introduced and its implementation explained.

5.1 WHfast

Rebound is specifically designed for astrophysical simulations and provides a range of integration schemes, including several symplectic integrators suitable for long-term orbital dynamics. In particular, Rebound includes an efficient and flexible implementation of the Wisdom-Holman integrator, known as WHFast, which is optimised for high performance and long-term energy conservation. The Kepler solver is unbiased, and its accuracy is improved using a high-accuracy implementation of c- and G-functions (which are used to compute the f- and g-functions introduced in the theory section), using a Laguerre-Conway solver for highly eccentric orbits, and by improving the convergence criteria for the Newton-Raphson method, and it ensures reversibility of coordinate transforms at the bit level, which decreases long-term energy drift. Its speed improvement over most regular implementations ranges from $1.5 - 5$ times faster[7]. The library allows the use of multiple different coordinate transforms, of which the Jacobi and Democratic-Heliocentric methods will be used [6].

5.2 Simulation parameters

The base units used for each simulation are astronomical units AU for distance, years yr for time, and solar masses M_{sol} for the mass. Rebound can add particles to a simulation from the NASA JPL Horizons database [6], all celestial bodies in the simulations will be added using their positions in this database at time 00:00 GMT 01-01-2000, which is $t = 0$ in all simulations. Rebound's own functions will be used to get positions, semi-major axes, eccentricities, orbital periods, and the total energy of the system.

6 Error Behavior

In Section 3, it was explained that the Wisdom-Holman integrator has a second-order error, e.g., its global error scales as $\mathcal{O}(\Delta t^2)$. Of course, this is the theoretical relation, which might only hold for the very small Δt limit. At the same time, as explained before, it is also the large Δt behaviour of the error we should be interested in. To investigate the behavior of the global error, the Wisdom-Holman simulations will be run in Python using the Rebound package, and the relative errors in eccentricity, semi-major axis, and total energy of the system will be analyzed. In this section, the test system will be introduced, and the error will be analysed for the small Δt limit and across a broader interval of Δt's. In all simulations in this section, Jacobi coordinates are used for the Wisdom-Holman integrator (a comparison between the Jacobi coordinates and Democratic-Heliocentric coordinates will follow in section 8). All errors in this section will be (absolute) relative errors defined by the following formula.

$$\text{Error} = \left| \frac{\textit{Experimental Value}}{\textit{Real Value}} - 1 \right| \tag{60}$$

Here *Real Value* is an approximation of the real value obtained by using a much smaller time step.

6.1 The Test System

We use a test system consisting of the Sun, Jupiter, Uranus, and Pluto: a simplified but dynamically rich subset of the Solar System that allows us to capture any long-range perturbative effects while remaining computationally tractable and avoiding any mean motion resonances. For the Jacobi coordinates, the obvious indexing order of Sun-Jupiter-Uranus-Pluto is taken, as clearly the orbits all lie neatly within one another and no crossings happen. The analyses of the relative errors in eccentricity and semi-major axis will be done on Pluto. This is done because Jupiter's and Uranus' eccentricity are both approximately $e = 0.05$ as opposed to Pluto's eccentricity of approximately $e = 0.24$ [13], meaning any small change in the eccentricity of the two gas giants has a high relative error, which could lead to data points becoming chaotic. In contrast, Pluto's higher eccentricity ensures more stable data on eccentricity errors. And for consistency, when looking at the error in the semi-major axis we will again look at Pluto.

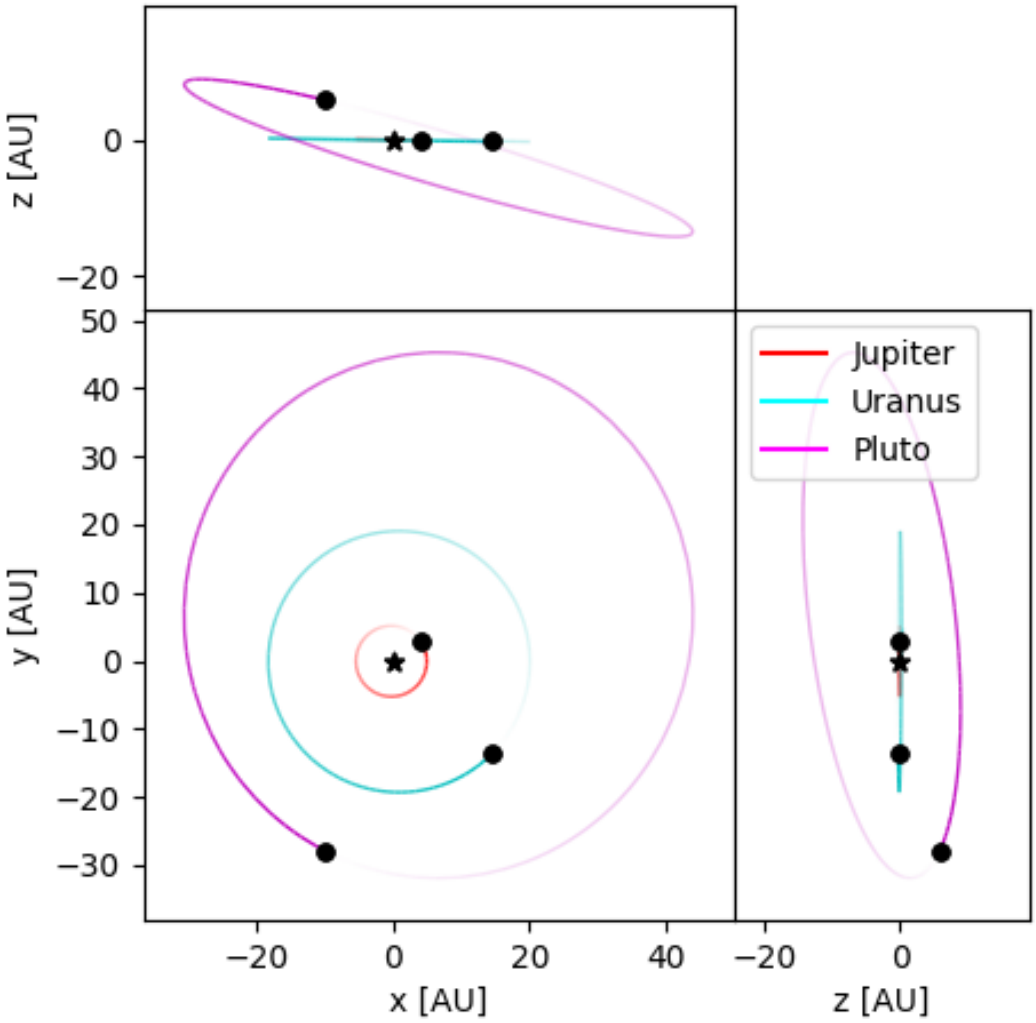

Figure 9: Orbital configuration of the test system used in the error simulations, consisting of the Sun (black star), Jupiter (red orbit), Uranus (cyan orbit), and Pluto (magenta orbit). The orbits are shown in projection onto the xy-, xz-, and yz-planes in astronomical units (AU). Black dots indicate the initial ($t = 0$) positions of the planets.

6.2 Small time step Δt Limit

For the small Δt limit of the error, a max timestep of $\Delta t \approx 5yr$ is taken, the total runtime of the simulation T is set equal to this largest timestep $T = max(\Delta t) \approx 5yr$. All the other timesteps of

$\Delta t \approx$ used are divisors of T, which ensures each simulation has the same total run time. These values can be found in the appendix. For the approximation of the exact result, a simulation with a time step of $\Delta t = 0.001 yr$ is used. This gives the result shown in Figure 10.

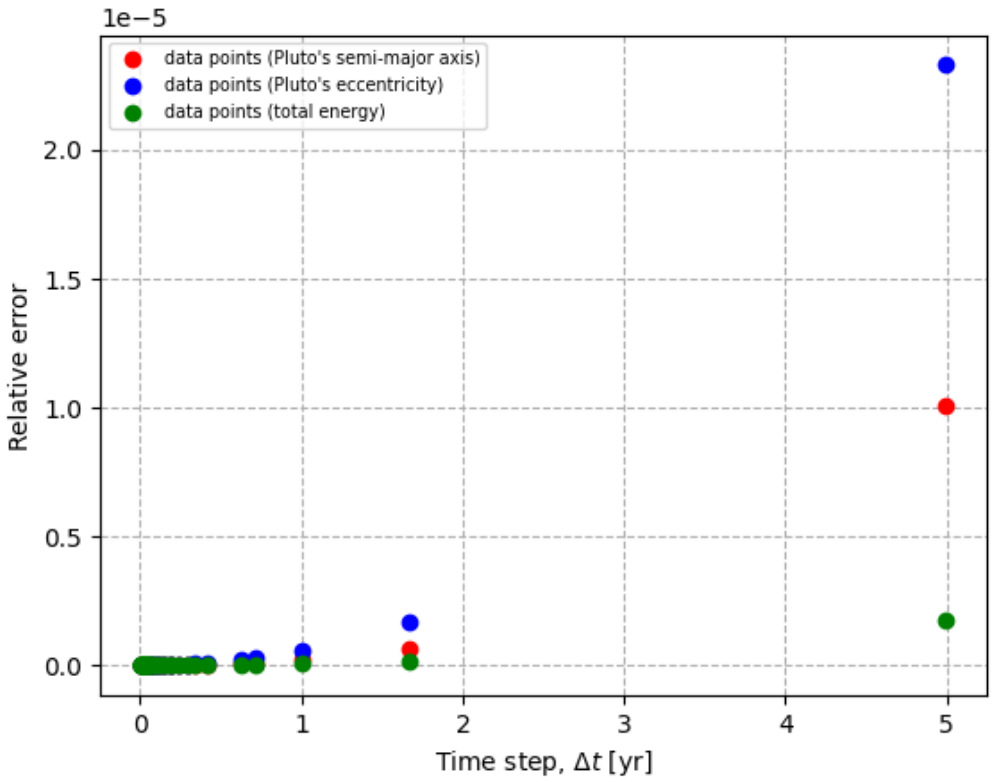

Figure 10: Relative errors in the semi-major axis and eccentricity of Pluto, as well as the total energy of the Sun-Jupiter-Uranus-Pluto system, as a function of the time step Δt in years, using the Wisdom-Holman integrator with Jacobi coordinates, in the small Δt limit. The errors are computed as the absolute value of the relative error and seem to exhibit a dependence on the time step.

We expect the Wisdom-Holman integrator to have a second order error, meaning that in the small Δt limit, the Δt^2 term of the error is expected to dominate. So the data should follow a power law of the form $Error(\Delta t) = a\Delta t^p$ where we expect $p = 2$. But it is clear that when performing a curve-fit on this data, the larger values for the higher Δt will dominate. Therefore, it is much more useful to plot this data in a log-log scale where a power law should form a straight line and perform a linear fit on the data. The formula used for the curve-fit is as follows:

$$\log_{10}(\text{Error}(\Delta t)) = p \cdot \log_{10}(\Delta t) + \log_{10}(a) \tag{61}$$

Plotting the data on a log-log scale and performing the curve-fits gives the result shown in Figure 11:

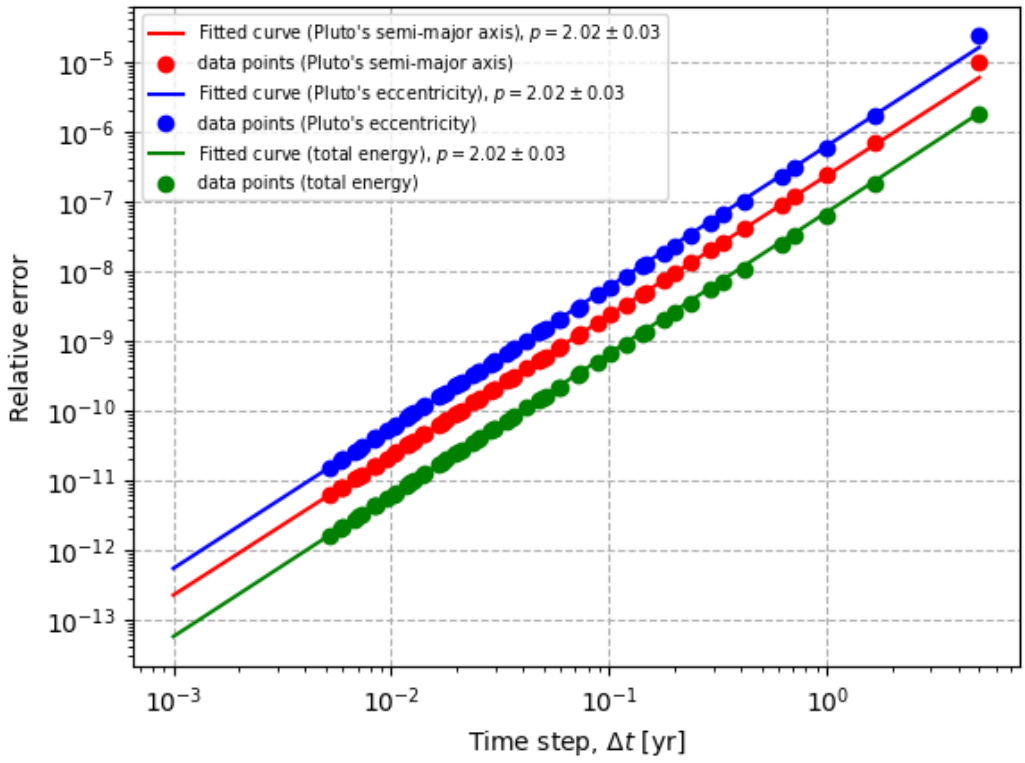

Figure 11: The data as in Figure 10 but now plotted on a log-log scale, with a linear curve-fit done on the data on a log-log scale. On a linear scale, the fitted curves follow a power-law scaling of the form $a\Delta t^p$, where p is the estimated order of the error. In all three cases, $p = 2.02 \pm 0.03$ was found.

For a second-order integrator, the expected value for p when looking at small Δt is $p = 2$, so the result, which in all three cases gives $p = 2.02 \pm 0.03$ agrees with this expectation. This provides strong numerical evidence that the Wisdom-Holman integrator is indeed a second-order numerical method in practice.

6.3 Broader Δt Interval

We will now look at what happens to the error when much bigger values of Δt are taken. Now $T = max(\Delta t) \approx 8 \cdot 10^3 yr$ and like before, all other Δt are divisors and can be found in the appendix. For the approximation of the exact result, a simulation with a time step of $\Delta t = 0.01 yr$ is used. This gives the result shown in Figure 12.

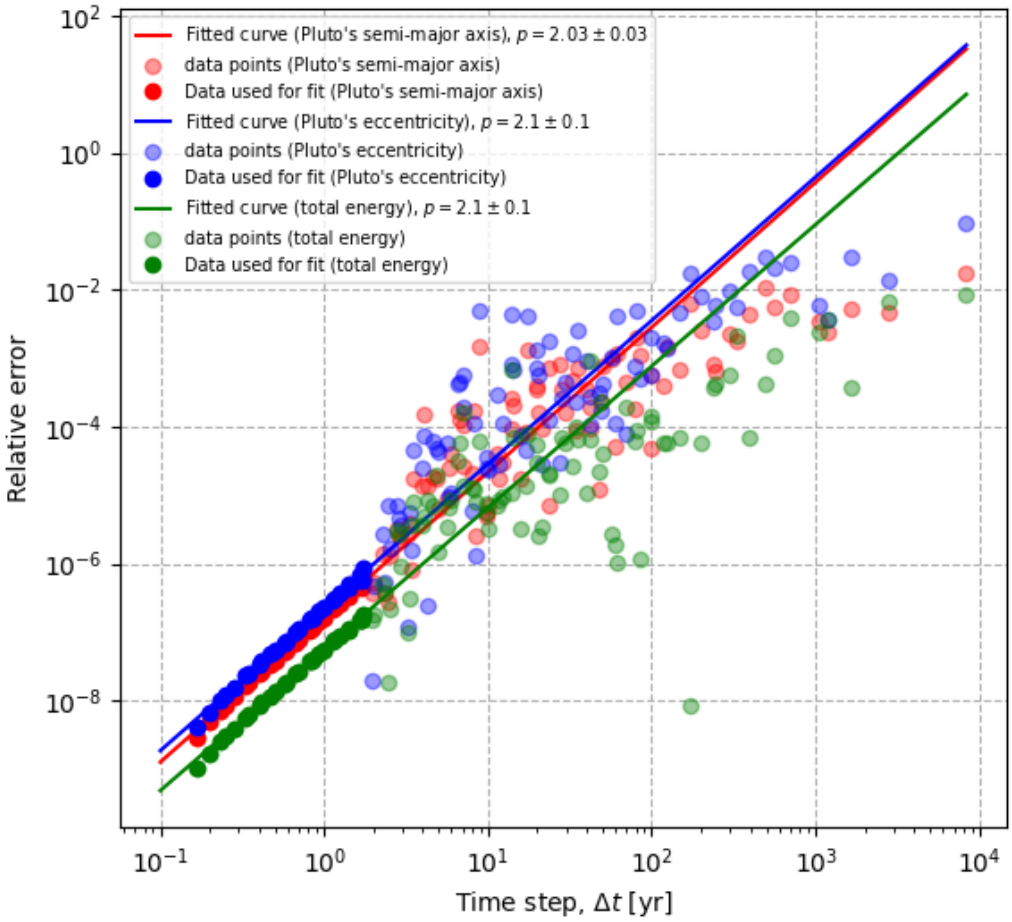

Figure 12: Relative errors in the semi-major axis and eccentricity of Pluto, as well as the total energy of the Sun-Jupiter-Uranus-Pluto system, as a function of the time step Δt in years, using the Wisdom-Holman integrator with Jacobi coordinates, for a long range of Δt. With curve-fits done on the data points of the lower Δt where the data appears to follow a clear power law and does not yet have a big spread indicating chaotic behavior. The points taken into account in the curve fit are highlighted in bold, while the other data points are displayed with a lower opacity. The fitted curves follow a power-law scaling of the form $a\Delta t^p$, where p is the estimated order of the error. In the case of Pluto's semi-major axis, $p = 2.03 \pm 0.03$ was found. For the other two errors, a value of $p = 2.01 \pm 0.01$ was found.

Once again, the data are consistent with the expected second-order error, and again, the error behaves very similarly across all three metrics. However, as shown in the figure, not all data points

can be accounted for in the curve fits performed for the larger time steps (in this case, at $\Delta t > 2yr$), where the error remains relatively small but becomes chaotic. It appears that the error behavior approaches a lower order for the high Δt. Only here, a curve fit is more difficult as there isn't a clear point where this has happened in the data, like there is with the second-order relation for the lower Δt (where it can still be argued that somewhat arbitrary points have been taken for the curve fit). To address this issue (and also the issue of selecting seemingly arbitrary points for our curve fit at the lower Δt), we will examine an even broader range of Δt, where the behavior for the larger Δt is expected to become more apparent.

6.4 Behavior up to very high Δt

We will now look at what happens to the error when much bigger values of Δt are taken. Now $T = max(\Delta t) \approx 5 \cdot 10^5 yr$ and like before, all other Δt are divisors and can be found in the appendix. For the approximation of the exact result, a simulation with a time step of $\Delta t = 0.1yr$ is used. This gives the result shown in Figure 13.

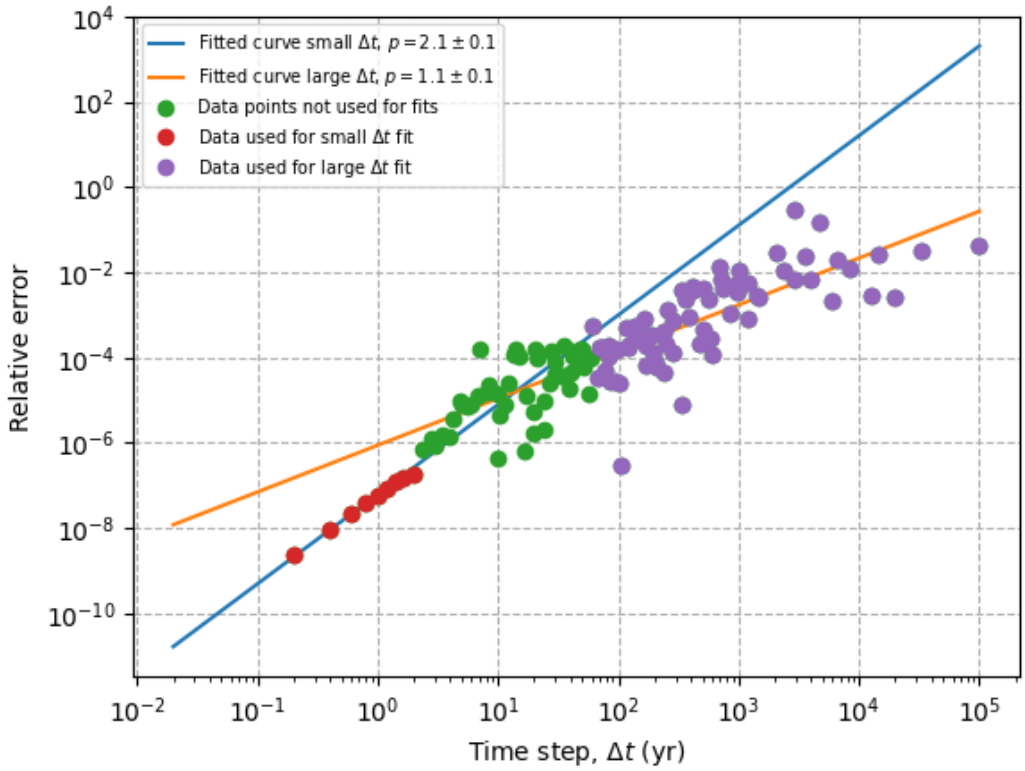

Figure 13: Relative errors of the total energy of the Sun-Jupiter-Uranus-Pluto system, as a function of the time step Δt in years, using the Wisdom-Holman integrator with Jacobi coordinates, for a very long range of Δt. With curve fits (following a power-law scaling of the form $a\Delta t^p$, where p is the estimated order of the error) done on the data points of the lower Δt (in red), where the data seems to follow a clear power law like in the previous figures, and a curve fit done on the larger Δt (in purple), where a power law also seems apparent. The fitted curves follow a power-law scaling of the form $a\Delta t^p$, where p is the estimated order of the error. For small Δt the previously observed second-order behavior is again observed ($p \approx 2.1 \pm 0.1$). However, for large Δt, the error seems to follow a different power law with $p \approx 1.1 \pm 0.1$, indicating a distinct error scaling regime.

For the small Δt, the second-order error is again apparent, as a curve fit on the first 10 data points gives a result of $p = 2.1 \pm 0.1$. However, we now also observe that for the larger time steps, there appears to be a clear power law once again, albeit of a lower order, which could be due to the orbital averaging effect (described in Section 4) maintaining accuracy even when the time steps get very large. In this case, a curve fit of the last 75 data points yields a result of $p = 1.1 \pm 0.1$. However, as before, the problem remains that a seemingly arbitrary number of data points was used in these curve fits. To investigate whether there truly are two distinct error scaling regimes, a new function is required that can account for all data points and allows for a smooth transition between power

laws. A function often used for this purpose, especially in the field of astrophysics (but mostly in the context of fitting empirical data of light intensity), is the Beuermann function [21, 22]:

$$Error(\Delta t) = A \left(\frac{\Delta t}{\Delta t_k} \right)^{\alpha} \left(1 + \left(\frac{\Delta t}{\Delta t_k} \right)^{1/\delta} \right)^{(\beta-\alpha)\delta} \tag{62}$$

In this expression:

- A is the normalization constant, setting the overall amplitude of the function.
- Δt_k is the break point or characteristic scale where the transition between the two power-law regimes occurs.
- α is the order of the error in the regime $\Delta t \ll \Delta t_k$ (the slope before the break).
- β is the order of the error in the regime $\Delta t \gg \Delta t_k$ (the slope after the break).
- δ controls the smoothness of the transition between the two regimes. Smaller values of δ result in a sharper transition; larger values produce a smoother transition.

Once again, to make it so the data points for the larger Δt don't dominate, and because the data is plotted on a log-log scale, the curve fit will be done using the log of this function:

$$\log_{10}(\text{Error}(\Delta t)) = \log_{10}(A) + \alpha \cdot \log_{10} \left(\frac{\Delta t}{\Delta t_k} \right) + (\beta - \alpha)\delta \cdot \log_{10} \left(1 + \left(\frac{\Delta t}{\Delta t_k} \right)^{1/\delta} \right) \tag{63}$$

This gives the result shown in Figure 14.

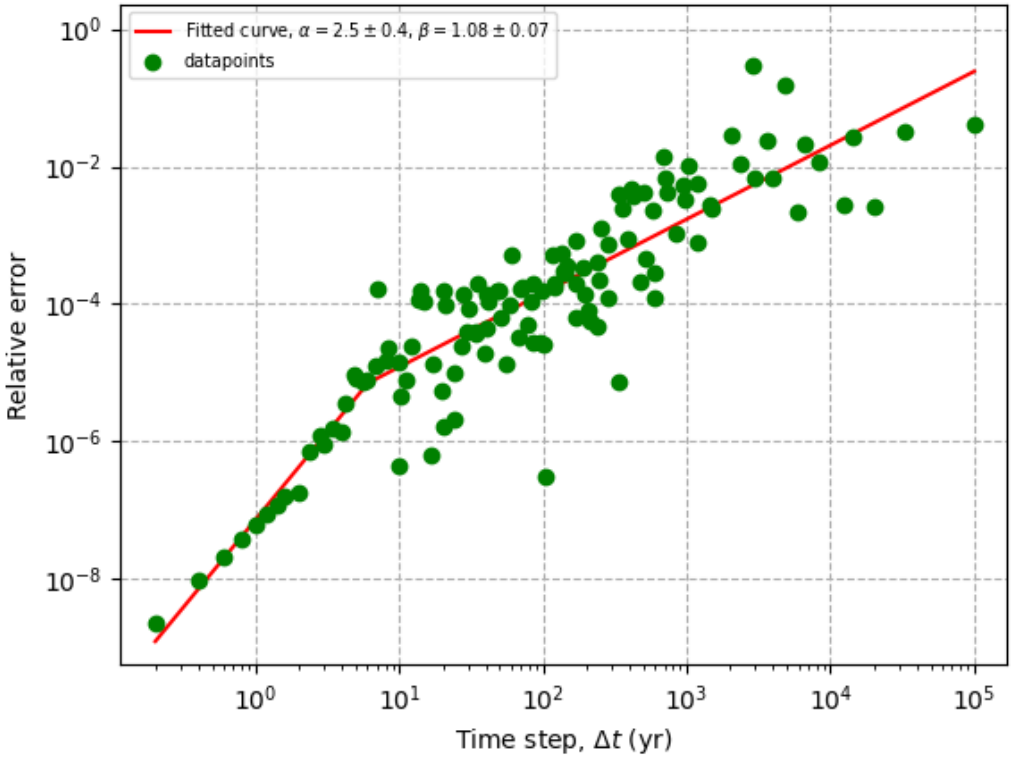

Figure 14: Relative errors of the total energy of the Sun-Jupiter-Uranus-Pluto system, as a function of the time step Δt in years, using the Wisdom-Holman integrator with Jacobi coordinates, for a very long range of Δt. A curve fit was done on the whole data set using the Beuermann function. And the fitted parameters of interest here are α (which is the order of the error for the small Δt), and β (the order of the error for the large Δt). We find $\alpha = 2.5 \pm 0.4$, which is close to the expected second-order behavior of the error in the small Δt limit. And we find $\beta = 1.08 \pm 0.07$, which agrees with the findings of the order of the error for the large Δt in the previous figure. This shows clearly that there are indeed two different error scalings.

The result of $\alpha = 2.5 \pm 0.4$ is slightly above the expected $\alpha = 2$ but still largely agrees with the second-order behavior of the error at the smaller Δt values. $\beta = 1.08 \pm 0.07$ suggests that the lower order error scaling for larger Δt that we found before is indeed correct; this is very significant as it means that for increasing Δt at a certain point in this case the error starts increasing linearly instead of quadratically, which means large time steps can be taken while still having an acceptable error. The break point was found to be $\Delta t_k = 6 \pm 2$ which means the switch from the second order to first order scaling of the error happens quite, before Δt surpasses the shortest period in the system $\mathsf{T}_{Jupiter} \approx 11yr$ [13]. The smoothness of the break was found to be $\delta = 0.01 \pm 0.01$, indicating that the break is very sharp and the transition between different scaling regimes occurs

abruptly. In the figure it can be seen that in this case, for $\Delta t \approx 10^3 yr$ we get $Error \approx 10^{-2}$, this means that in this simulation a Δt of about a hundred times the shortest period in the system (in this case Jupiter's) only leads to an error of about 1%. In this case, the total runtime wasn't very high, being of the order 10^5 instead of the 10^6 to 10^9 that one might want to use. But it does still show that even for considerably large time steps, the resulting error can still be acceptable.

7 Error Behavior In Resonant Systems

In the previous section, we examined how the error behaves in a test system that did not include any mean motion resonances. However, these occur frequently in nature, so understanding the error behavior in systems containing resonances is essential. We will (as in the last section) examine how the errors behave under different Δt values, and we will investigate how the ratio of the orbital periods changes over time using various Δt values, thereby assessing how well the libration is preserved.

7.1 The Test System

We use a test system consisting of the Sun, Neptune, and Pluto. This system has a 3:2 mean motion resonance as explained in subsection 2.2. We have excluded the rest of the Solar system to ensure we are solely focusing on the two resonant bodies, and thus we don't have to worry about perturbations from other planets. The two orbits cross, but, as explained earlier, the mean motion resonance shields Pluto from any close encounters with the gas giant. Such a system can be pretty delicate because if the error over a single timestep (or the error accumulating over a few time steps) becomes too large and pushes the system beyond the edge of its restoring potential, the period of Pluto might begin to drift (any significant changes in orbital elements will be for Pluto as Neptune's mass is about four orders of magnitude greater). Eventually, this could lead to a close encounter with Neptune. This would cause significant changes to the system, which in fact should be stable over billions of years [15]. For the Jacobi Coordinates, the indexing order Sun-Neptune-Pluto is used, because even though the two orbits do cross, Neptune is well within Pluto's orbit for most of the time.

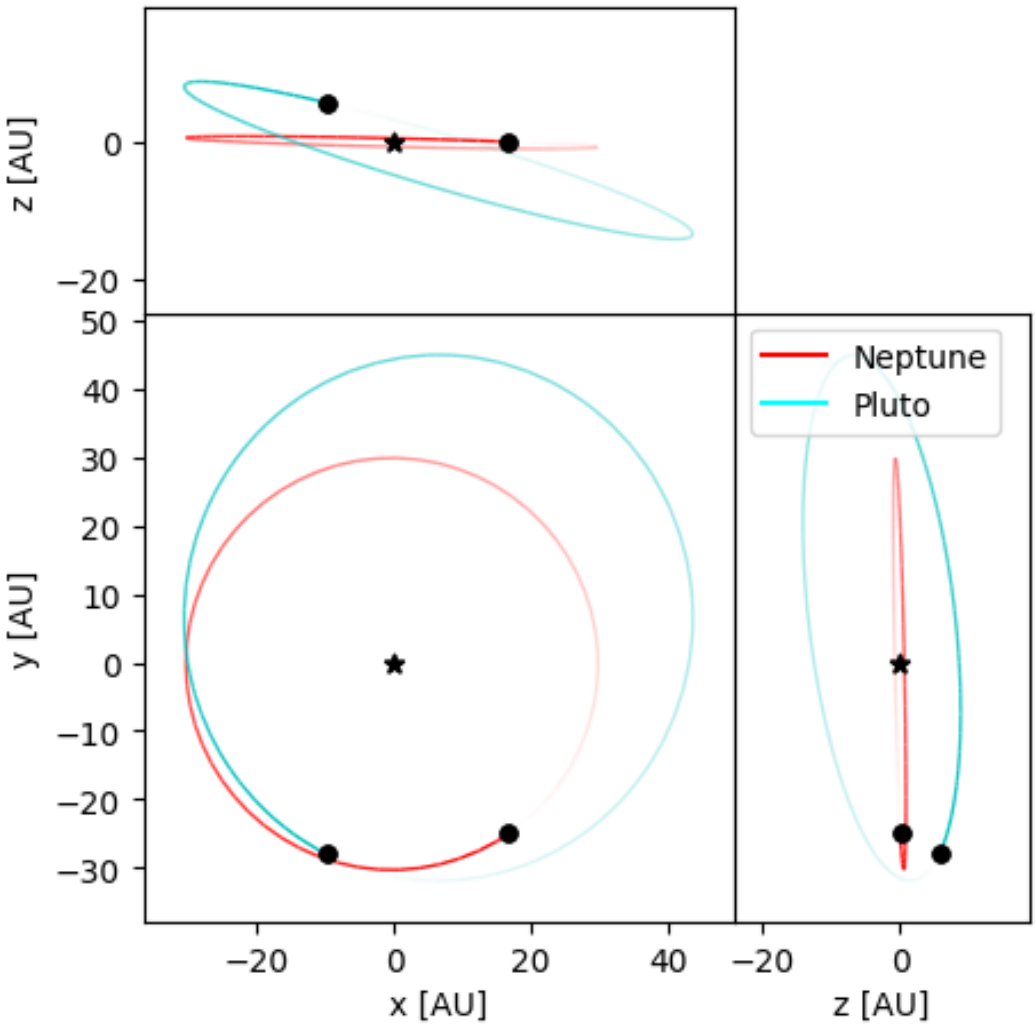

Figure 15: Orbital configuration of the test system used in the error simulations, consisting of the Sun (black star), Neptune (red orbit), and Pluto (cyan orbit). The orbits are shown in projection onto the xy-, xz-, and yz-planes in astronomical units (AU). Black dots indicate the initial ($t = 0$) positions of the planets.

7.2 Error behavior over a range of Δt

We will examine the error in the same manner as in subsection 6.4. But this time, we won't be able to focus on the error in the total energy of the system. This is because the total energy is almost solely dominated by Neptune's energy, which will remain relatively constant even if there is a massive error in Pluto's orbit. We will therefore examine the error in the eccentricity of Pluto, which in this case is a much better metric of how well the system's configuration is preserved. Again, we use $T = max(\Delta t) \approx 5 \cdot 10^5 yr$ and, like before, all other Δt are divisors and can be found in the appendix. Do keep in mind that the shortest period in this system is an order of magnitude bigger than the shortest period in the system used in subsection 6.4, so a bigger timestep here (in yr) isn't necessarily a bigger timestep relative to the timescale of the system at hand. For the approximation of the exact result, a simulation with a time step of $\Delta t = 0.1 yr$ is used. And again, a Beuermann function will be fitted to the data. This gives the result shown in Figure 16.

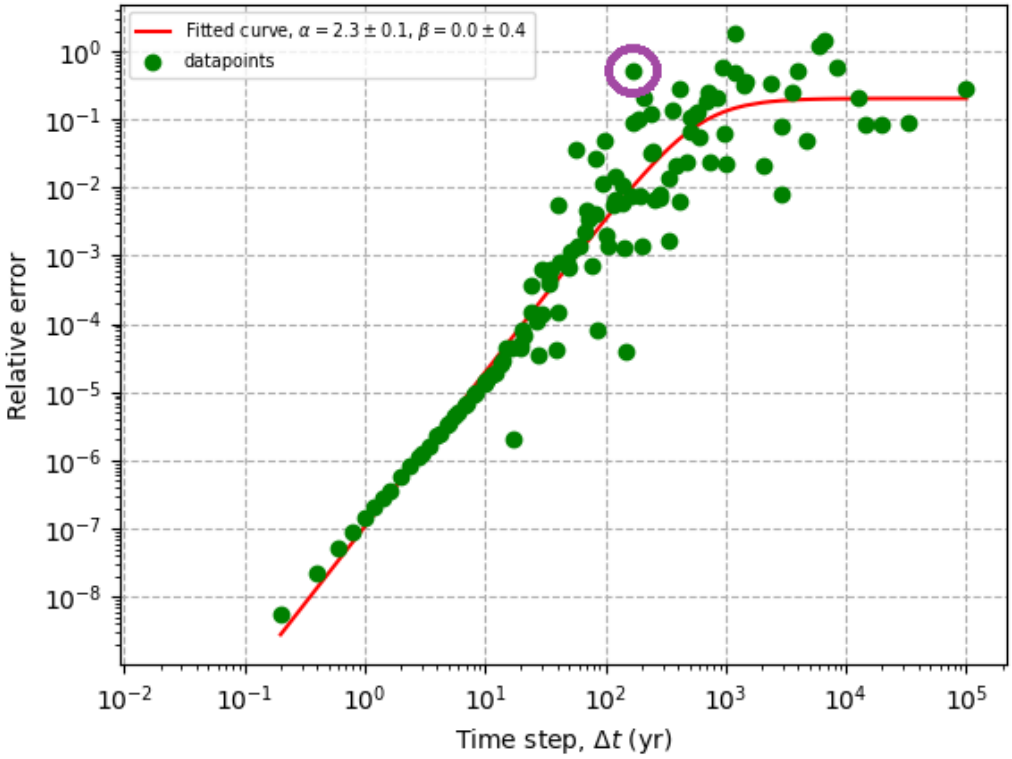

Figure 16: Relative errors in the eccentricity of Pluto in a Sun-Neptune-Pluto system, as a function of the time step Δt in years, using the Wisdom-Holman integrator with Jacobi coordinates. A curve fit was done on the whole data set using the Beuermann function. And the fitted parameters of interest here are α (which is the order of the error for the small Δt), and β (the order of the error for the large Δt). We find $\alpha = 2.3 \pm 0.1$, which is close to the expected second-order behavior of the error in the small Δt limit. And we find $\beta = 0.0 \pm 0.4$, so once again at a certain point the error becomes of a lower order. The data point circled in purple is of particular significance, as it is a big outlier in the data, and for this datapoint $\Delta \approx \mathsf{T}_{Neptune}$

Again, the second-order behavior of the Wisdom-Holman integrator at the small Δt limit is confirmed with a finding of $\alpha = 2.3 \pm 0.1$. Again, the order of the error decreases after a certain breakpoint, although due to the break happening quite late, the numerical evidence for this lower order is weaker than before (reflected in the larger uncertainty in β). Notably, in this case the error (in the relevant metric in this case eccentricity of Pluto as opposed to the total energy of the system) reaches a 10^{-2} an order of magnitude sooner than it did in subsection 6.4, and because the timescale of this system is an order of magnitude larger it means that relative to the timescale of this system the error of 10^{-2} happens two orders of magnitude sooner than it did in the non resonant system of the last section (in this case around $\Delta t \approx 10^2$, which is smaller than the shorter

period in the system $\mathsf{T}_{Neptune} \approx 165yr$ [13]). This could be because the orbits intersect. So if an accumulation of error brings the system out of its resonance, the error can increase quite quickly due to possible closer encounters between Pluto and Neptune. Another interesting finding is the outlier in the error at $\Delta t \approx \mathsf{T}_{Neptune}$. This significantly larger error is likely caused by the fact that, in this case, not only is Neptune at the same position at each moment in discrete time, but also, since the system is in resonance, Pluto is constantly in one of two positions that are also constant. Hence, there is no orbital averaging, which results in the kicks having an accumulating effect, leading to a larger error. This introduces a topic which, especially for systems in resonance (due to the periodicity of the system), is of great importance, namely step size resonance [23].

7.3 Step Size Resonance

When the time step closely matches a natural frequency or divisor/multiple of a natural frequency of the system, we say the time step resonates with that natural frequency. This can lead to numerical artifacts when the system is integrated over multiple time steps; a phenomenon known as step size resonance (also referred to as numerical resonance) [24].

7.3.1 Resonance with Orbital Periods

When the integration step size Δt is close to a rational multiple or divisor of an orbital period T of one of the bodies, the numerical error introduced at each time step can accumulate coherently. This phenomenon is analogous to driving a pendulum at its natural frequency: small nudges at the right time add up. In the context of orbital dynamics, this manifests as an artificial secular drift or oscillation in the orbital elements of the affected body [25]. More specifically, step size resonances can occur when

$$\Delta t \approx \frac{\mathsf{T}}{n} \quad \text{or} \quad \Delta t \approx n\mathsf{T} \tag{64}$$

for some small integer n. In these cases, the integration samples the orbit at the same phase repeatedly, leading to a reinforcement of numerical error patterns. The most severe cases typically occur when Δt is a subharmonic of the orbital period, such as $\Delta t = \mathsf{T}/2$ or $\mathsf{T}/3$.

7.3.2 Amplification in Mean Motion Resonances

The situation becomes more problematic when the planetary system contains bodies in a mean motion resonance (MMR), such as Pluto and Neptune.
A poorly chosen step size can interfere with this delicate dynamical balance. Suppose the step size is close to a multiple or subharmonic of the libration period or the orbital periods of the resonant bodies. In that case, the integrator may consistently over- or under-sample certain parts of the resonance cycle. This can distort the dynamics of the resonant angle, leading to artificial growth or decay of the libration amplitude. Over long timescales, it's reasonable to assume such resonant artifacts may lead to: spurious chaotic behavior, false resonance breaking, or energy drift.

7.3.3 Practical Implications

In practical integrations—such as those involving Pluto and Neptune or other tightly coupled systems—care must be taken to ensure that the time step Δt avoids simple fractional ratios with any orbital period or resonant cycle.

7.3.4 Testing the Step Size Resonance

To examine how noticeable these time step resonances are, we again compute the error with multiple different Δt, only this time the total duration is taken to be $T = \mathsf{T}_{Pluto} \cdot \mathsf{T}_{Neptune}$, this means that $\frac{\mathsf{T}_{Pluto}}{n}, \frac{\mathsf{T}_{Neptune}}{n} \quad i \in \{1, 2, 3, 4, 5\}$ can be added to a list of divisors of T so if the step size resonance has an apparent effect we will be able to see it as outliers in the data. All the other divisors can be found in the appendix. For the approximation of the exact result, a time step $\Delta t \approx 0.1yr$ is taken. This gives the result shown in Figure 17.

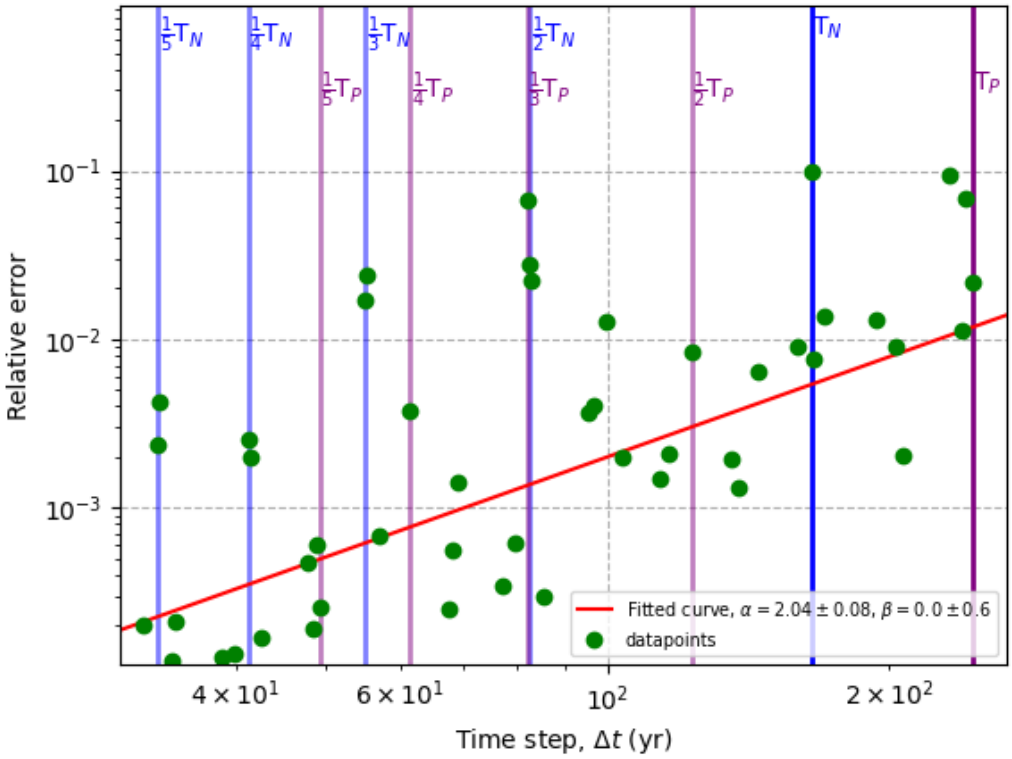

Figure 17: Relative errors in the eccentricity of Pluto in a Sun-Neptune-Pluto system, as a function of the time step Δt in years, using the Wisdom-Holman integrator with Jacobi coordinates. Zoomed in on the first sub-harmonics of the orbital periods. A curve fit was done on the whole data set using the Beuermann function. And the fitted parameters of interest here are α (which is the order of the error for the small Δt), and β (the order of the error for the large Δt). We find $\alpha = 2.04 \pm 0.08$, and $\beta = 0.0 \pm 0.6$. The vertical lines are the lines $\Delta t = \frac{\mathsf{T}_{N,P}}{n}$, for $n \in \{1, 2, 3, 4, 5\}$, Where $\mathsf{T}_{N,P}$ are the orbital periods of Neptune and Pluto respectively. It's clear that the error spikes at and around these values, indicating that step size resonance can indeed induce large errors.

In the figure, it is clear that at almost all subharmonics (all except $\frac{\mathsf{T}_{Pluto}}{5}$), the error does indeed spike. This is a clear indication that step size resonance can induce significant errors, Which means that when taking larger timesteps, it is vital to make sure none of these divide the natural frequencies of the system.

7.4 Conserving the Mean Motion Resonance

We have now examined how the global error of a system in mean motion resonance varies with step size. But maybe of even bigger importance is if the integration conserves the resonance, as the resonance is a very important attribute of the system and has a huge impact on its configuration long term. Of secondary importance is to see how well the oscillation in the libration of the resonance is conserved. To test how well the Wisdom-Holman integrator conserves these attributes, we will run multiple long term simulations (at different Δt) and track the evolution of $\frac{\mathsf{T}_{Neptune}}{\mathsf{T}_{Pluto}}$ over time. The orbital periods are calculated from the semi major axis using the following formula $\mathsf{T} = 2\pi\sqrt{\frac{a^3}{GM}}$ [1], Here M is the mass of the central body. We will look at what happens in both the case step size resonance is avoided and the case where step size resonance is deliberately sought out.

7.4.1 Simulation Avoiding Step Size Resonance

Firstly we look at the case where none of the step sizes tried fall relatively near a subharmonic of the either one of the orbital periods. We take $\Delta t \in \{10, 90, 140, 180\} yr$. We approximate the exact solution with $\Delta t = 1 yr$. Over a total time $T = 80,000 yr$ This gives the result shown in Figure 18.

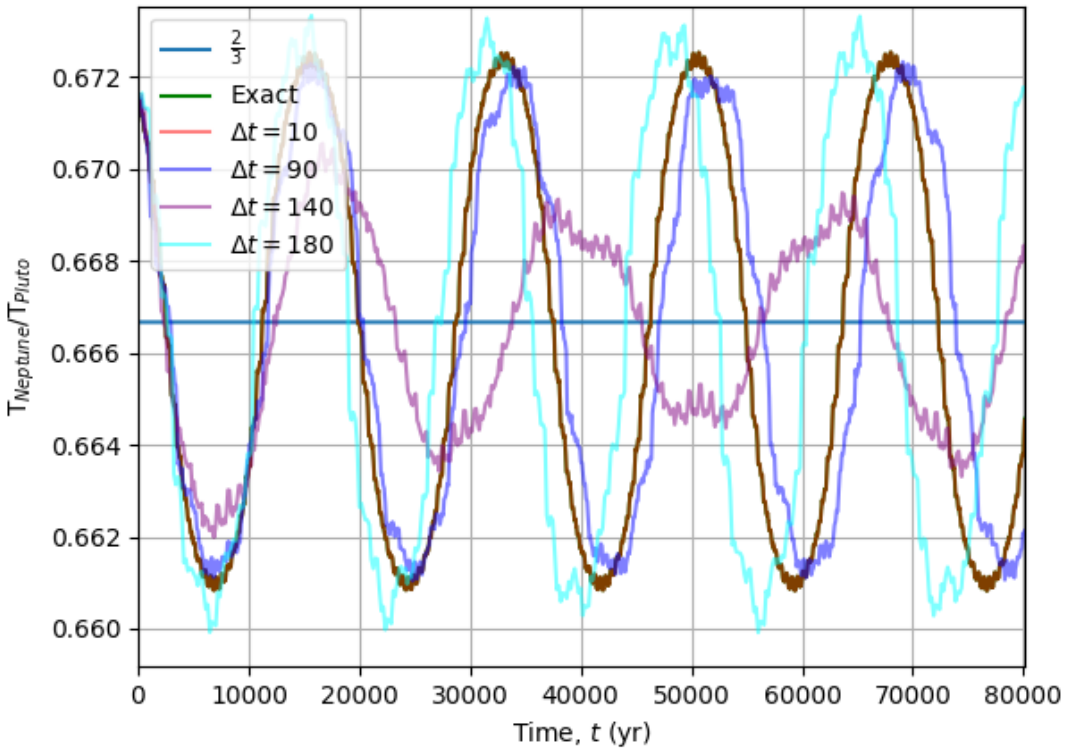

Figure 18: The ratio of the orbital periods of Neptune and Pluto, $\frac{T_{Neptune}}{T_{Pluto}}$, as a function of time t in years, computed using the Wisdom-Holman integrator with Jacobi coordinates. With a time step $\Delta t \in \{10, 90, 140, 180\} yr$. The horizontal blue line at $\frac{2}{3}$ is shown for reference, indicating the nominal 3:2 mean motion resonance. It's clear that for $\Delta t = 10 yr$ the mean motion resonance is still conserved very well as the red line lies on top of the green (exact) line. For the larger time steps the resonance is still maintained but the libration does not follow the exact solution quite as well anymore. And especially the result for $\Delta t = 140 yr$ is quite far off the exact solution

The figure shows that the Wisdom-Holman integrator is capable of maintaining the mean motion resonance, especially for $\Delta t = 10 yr$ is still very accurate showing that relatively larger time steps can still give an accurate result. For the other time steps show the result is interesting as it it clear that the time step size doesn't inversly correspond with how well it matches the exact solution, as it is clear that the solution for $\Delta t = 140 yr$ is a lot worse than the solution for $\Delta t = 180 yr$. The solution for $\Delta t = 180 yr$ shows that is possible to relatively accurately capture the resonance while the the time step is larger than the shortest orbital period of the system $T_{Neptune} \approx 165 yr$. To examine if $\Delta t = 180 yr$ still gives a better result than $\Delta t = 140 yr$ even on a large timescale, we will run the simulation for $T = 200,000 yr$ and compare them against the (approximatly) exact solution. This gives the result shown in Figure 19

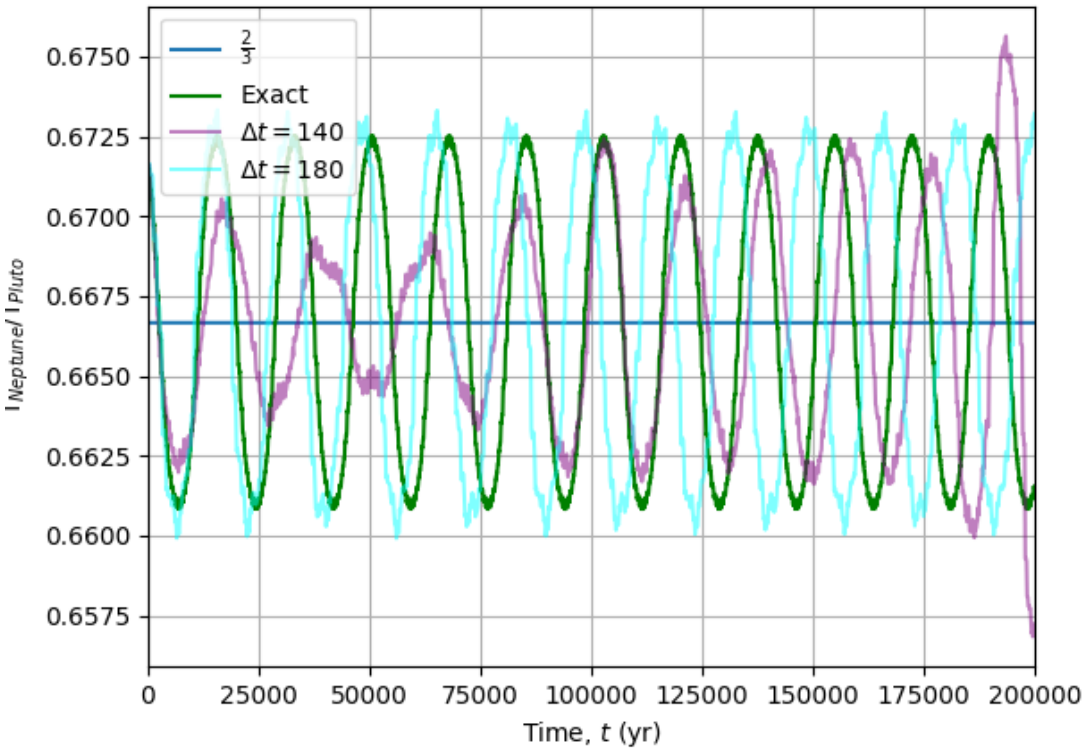

Figure 19: The ratio of the orbital periods of Neptune and Pluto, $\frac{\mathsf{T}_{Neptune}}{\mathsf{T}_{Pluto}}$, as a function of time t in years, computed using the Wisdom-Holman integrator with Jacobi coordinates. With a time step $\Delta t \in \{140, 180\} yr$. The horizontal blue line at $\frac{2}{3}$ is shown for reference, indicating the nominal 3:2 mean motion resonance. Even though for $\Delta t = 180 yr$ the libration period seems to be slightly shorter than the exact solution resulting in a slowly increasing phase shift, it's clear even over a longer runtime it's still vastly better than the unstable solution for $\Delta t = 140 yr$

It's clear that still the solution for $\Delta t = 180 yr$ preserves the resonance quite well even over the long term, it does show that the libration period is slightly shorter than the exact result resulting in a slowly growing phase shift between the two solutions over time. The solution for $\Delta t = 140 yr$ is clearly quite unstable suggesting that there might still be a step size resonance, which could be due to a multiple of this timestep possibly getting close to a multiple of one of the orbital periods, possibly in conjugation with an unfortunate location of the bodies at certain time steps. This shows that clearly the general structure of the resonant system can be conserved even for a time step larger than the shortest orbital period of the system, but one needs to get lucky with the choice in time step.

7.4.2 Simulation With Obvious Step Size Resonance

We will now look at what happens when a time is taken that is very close to a subharmonic of one of the orbital periods. We will look at the case $\Delta t = 82yr \approx \frac{\mathsf{T}_{Neptune}}{2}$, and $\Delta t = 123yr \approx \frac{\mathsf{T}_{Pluto}}{2}$. The exact solution is again approximated with $\Delta t = 1yr$, and the total runtime $T = 400,000yr$. This gives the result shown in Figure 20.

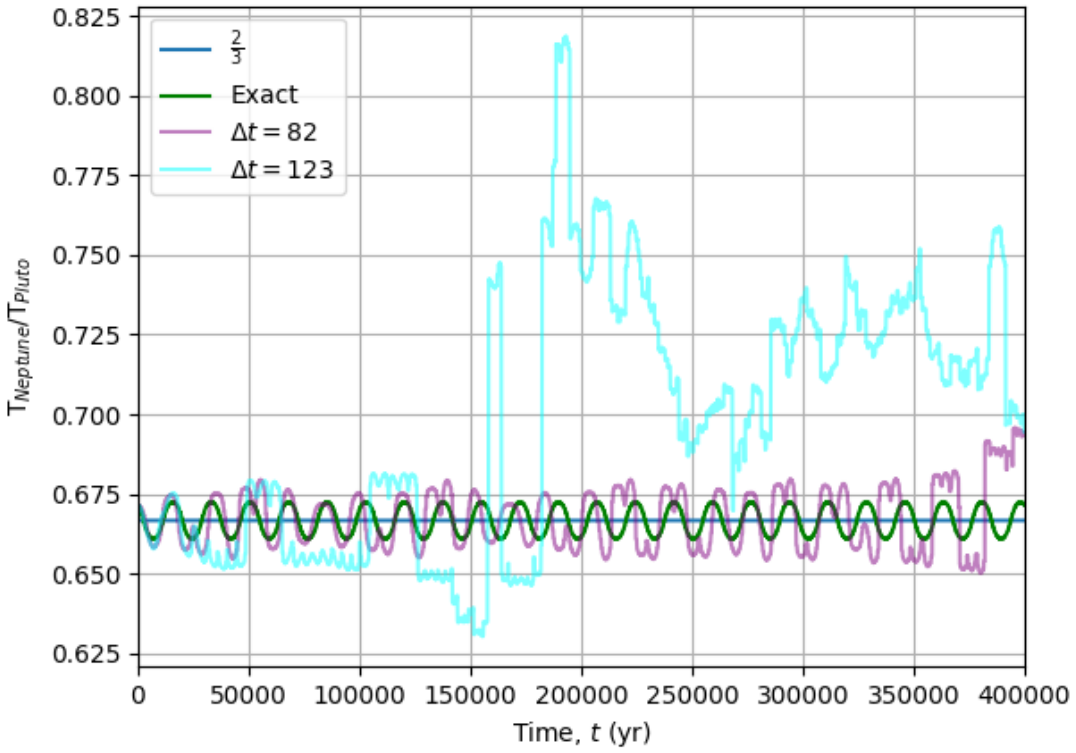

Figure 20: The ratio of the orbital periods of Neptune and Pluto, $\frac{\mathsf{T}_{Neptune}}{\mathsf{T}_{Pluto}}$, as a function of time t in years, computed using the Wisdom-Holman integrator with Jacobi coordinates. With a time step $\Delta t \in \{82, 123\}yr$. The horizontal blue line at $\frac{2}{3}$ is shown for reference, indicating the nominal 3:2 mean motion resonance. These two time steps show very obvious the effect step size resonance can have on a resonant system, as in both cases the libration does not at all resemble the exact solution, and it the case of $\Delta t = 123yr$ the resonance is quite clearly broken.

It's clear from the figure that step size resonance is something that definitely has to be taken into account when simulating a mean motion resonant system. As in both cases the libration doesn't resemble the exact solution at all, and in the case of $\Delta t = 123yr$ the resonance is obviously broken. In both cases the general structure of the system was obviously not conserved and thus any long term simulation would yield vastly inaccurate results, once again proving the importance of negating

these step size resonances.

8 Comparison Between Jacobi- and Democratic Heliocentric Coordinates

To compare the performance of Jacobi coordinates and Democratic Heliocentric coordinates, we will look at two different systems. The first is the Sun-Jupiter-Uranus-Pluto system introduced in section 6. This system is obviously very suitable for Jacobi coordinates as all orbits lie neatly within one another so there is a clear and always correct ordering of the bodies. The second system will is the Sun-Neptune-Pluto introduced in section 7. Here there is still a clear choice of ordering only since the orbits cross this ordering isn't always correct, making the system more suited for Democratic Heliocentric coordinates.

8.1 Clear Jacobi Coordinates Ordering

The system we use is the familiar Sun-Jupiter-Uranus-Pluto system, which is very suited for Jacobi coordinates given its obvious ordering. We compare the error between the two methods by comparing the result we got in subsection 6.4 using Jacobi coordinates, with the result we get if we run the exact same simulations but now using Democratic Heliocentric coordinates. This gives the result shown in Figure 21.

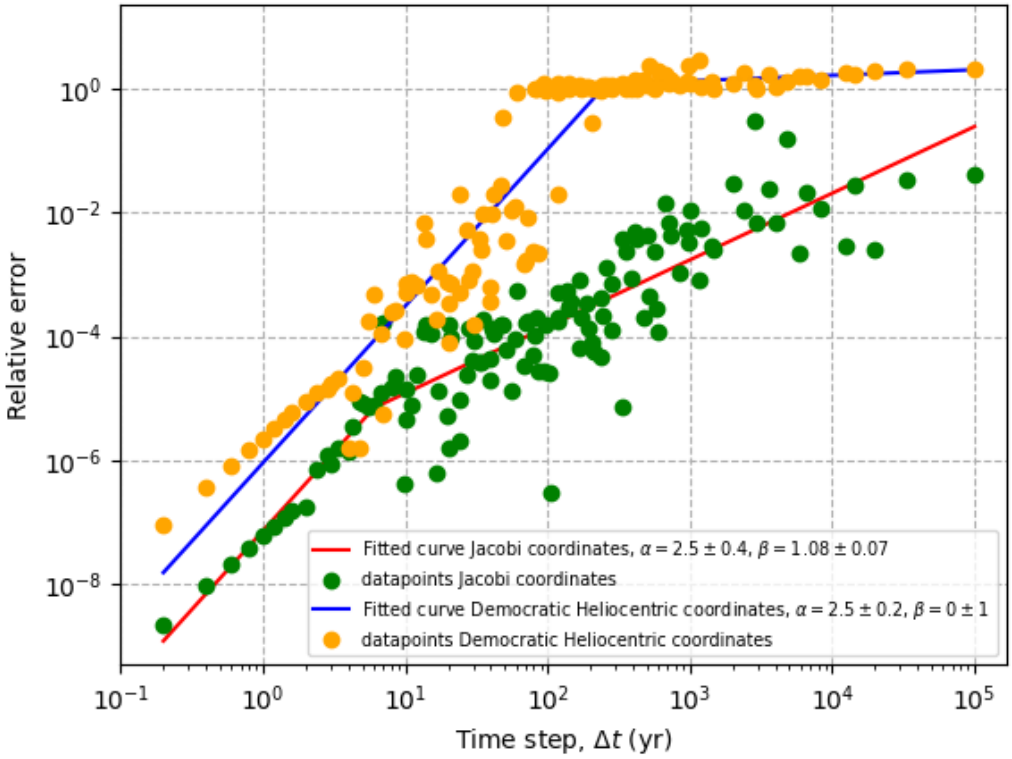

Figure 21: Similar to Figure 14, added are the errors (in total energy of the system) found using Democratic Heliocentric coordinates (orange), and a Beuermann function curve fit on this data (blue). For the Democratic Heliocentric coordinates $\alpha = 2.5 \pm 0.2$ was found which is similar to the $\alpha = 2.5 \pm 0.4$ found using Jacobi coordinates. The beta found using Democratic Heliocentric coordinates is quite different $\beta = 0 \pm 1$ instead of the $\beta = 1.08 \pm 0.07$ for the Jacobi coordinates, which means the error scales less quickly for the large Δt using Democratic Heliocentric coordinates (although this could also be due to the error seemingly plateauing around 1). Only the error gets above 100% before the break in the into a lower order error, so the errors for larger Δt are also significantly larger using Democratic Heliocentric coordinates as compared to the error using Jacobi coordinates It's clear that the error using Democratic Heliocentric coordinates is a lot higher, even for small Δt it is almost two full orders of magnitude larger

These results clearly show that for this system the error using Democratic Heliocentric coordinates is a lot worse than when using Jacobi coordinates. Not only does is it two full orders of magnitude higher in the small Δt limit, but the breaking point into a lower order of error only happens once the error has already reached/surpassed 100% meaning that at those Δt the system is already completely different to the real system and any such simulation would be completely useless. In fact, the break might be due to error plateauing around 100% where a bigger time step won't lead

to a larger error. The difference in error is so large that an error of around 10^{-2} is reached two full orders of magnitude sooner using Democratic Heliocentric coordinates than when using Jacobi coordinates (around $\Delta t \approx 10^1 yr$ as opposed to $\Delta t \approx 10^3 yr$). This all clearly shows that for systems with orbits neatly lying within each other, and thus with an obvious ordering for Jacobi coordinates, Jacobi coordinates do outperform Democratic Heliocentric coordinates by quite a large margin.

8.2 System without a clear ordering

Now, the system we use is the Sun-Neptune-Pluto system, which, given the crossing of the orbits, is expected to be better suited for Democratic Heliocentric coordinates. We compare the error between the two methods by comparing the result we got in subsection 7.2 using Jacobi coordinates, with the result we get if we run the exact same simulations but now using Democratic Heliocentric coordinates. This gives the result shown in Figure 22.

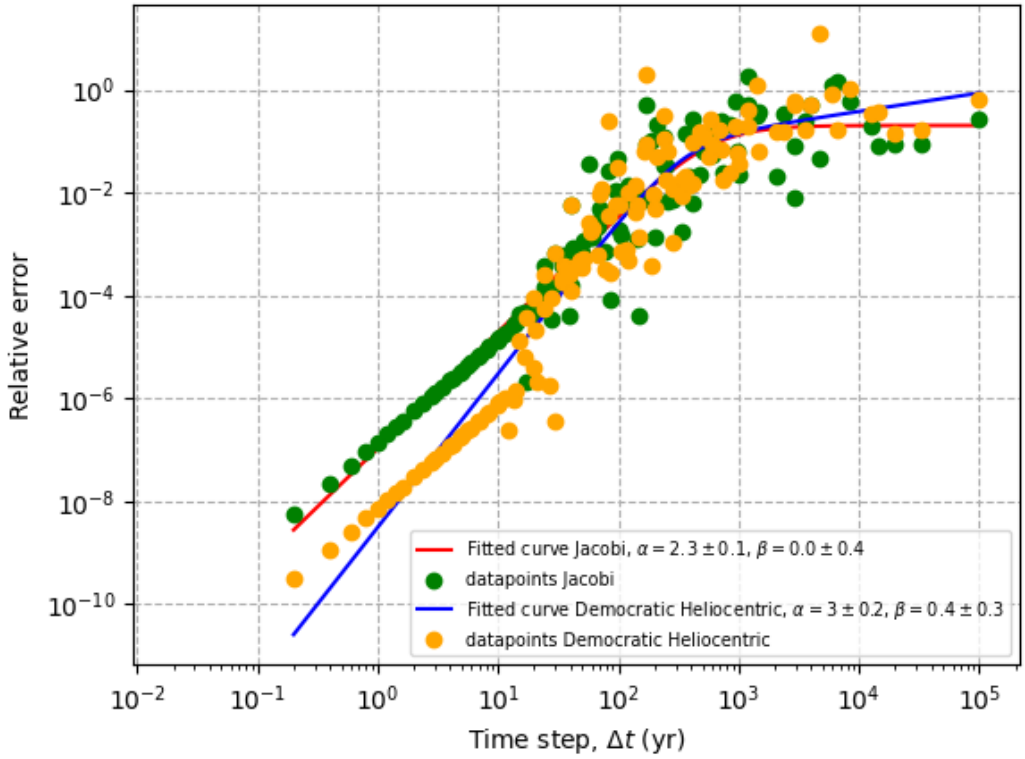

Figure 22: Similar to Figure 16, added are the errors (in total eccentricity of Pluto) found using Democratic Heliocentric coordinates (orange), and a Beuermann function curve fit on this data (blue). For the Democratic Heliocentric coordinates $\alpha = 3 \pm 0.2$ was found which differs from the $\alpha = 2.3 \pm 0.1$ found using Jacobi coordinates, but in the figure it can be seen that this power is too high for the beginning of the data which runs parallel to the data using the Jacobi coordinates showing that the error is still of the second order for the small Δt limit, meaning the Beuermann function can't fully capture this error behavior. The beta found using Democratic Heliocentric coordinates is relatively similar $\beta = 0.4 \pm 0.3$ instead of the $\beta = 1.08 \pm 0.07$ for the Jacobi coordinates. In both cases the break in the order of the error happens after the error has already gotten quite high 10^{-1}. For the smaller Δt, the error using Democratic Heliocentric coordinates is significantly smaller as compared to when using Jacobi coordinates, which shows that indeed systems like these are better suited for Democratic Heliocentric coordinates.

In this figure, it's clear that Democratic Heliocentric coordinates are better in the small Δt limit (the error is around two orders of magnitude lower) as expected for a system like this. For larger Δt, it seems like Democratic Heliocentric coordinates are slightly worse than Jacobi coordinates. Still, this switch only occurs after both methods have already encountered an error of around 10^{-1}, which is already too high to be truly useful. The fact that the error using Democratic Heliocentric

coordinates is higher for larger time steps might be because the orbit of a body (even in a two-body system) isn't exact using Democratic Heliocentric coordinates, which, over larger time steps, might introduce significant errors.

9 Conclusion

This thesis set out to investigate the practical performance of the Wisdom-Holman symplectic integrator, with an emphasis on its behavior across a wide range of time step sizes in both non-resonant and resonant planetary systems. Through systematic numerical experiments using the Rebound package, the error scaling, the influence of mean-motion resonances, step size resonances, and the impact of coordinate system choice were analyzed.
The results for the Sun–Jupiter–Uranus–Pluto system confirmed that, the Wisdom–Holman integrator exhibits second-order error behavior in the small time step limit, in line with theoretical expectations. Notably it showed that in the non resonant case, for larger time steps, a clear transition to a lower-order regime was observed. This supports the idea that orbital averaging helps maintain reasonable accuracy even when the step size exceeds the shortest orbital period. For long-term ensemble simulations, this means that computational costs can be reduced significantly by choosing time steps in this regime while still maintaining acceptable accuracy.
The simulations of the Sun–Neptune–Pluto system demonstrated that systems containing mean-motion resonances are far more sensitive. Here, the expected second-order behavior at small Δt again appeared, but the onset of significant error growth occurred at a relatively lower time step compared to the non-resonant system. The presence of step size resonances was clearly demonstrated: when the integration step size approached simple fractions or multiples of the resonant orbital periods, the error increased abruptly. This shows how choosing the wrong time step can potentially lead to spurious resonance breaking, and orbital instability..
In addition, this work compared the use of Jacobi coordinates and Democratic Heliocentric coordinates within the Wisdom–Holman scheme. The results showed that Jacobi coordinates generally yielded slightly lower energy drift and better long-term stability for hierarchical systems with a dominant central mass. Democratic Heliocentric coordinates, on the other hand, had more accurate results when the ordering of the bodies wasn't obvious. This demonstrates that the choice of coordinate system can have a measurable effect on accuracy and should be carefully matched to the physical structure of the system being studied.

Recommendations for future research. Building on these results, several directions for further research are recommended:

- **An algorithm to avoid step size resonances**: Develop an algorithm to find time steps which avoid step size resonances, this would enable the use of larger time steps, especially in the case where it isn't yet known of the systems contains any resonances.
- **Coordinate system optimization:** Develop guidelines or algorithms to choose the most appropriate Hamiltonian split(Jacobi, Democratic Heliocentric, or another) automatically, based on system architecture and orbital hierarchy.
- **Extending to realistic multi-planet systems:** Apply these methods to more realistic and complex configurations, such as the full Solar System or exoplanetary systems with multiple resonances, to validate the findings under real-world dynamical conditions.
- **Development of hybrid schemes:** Implement and test an integrator that combines the Wisdom–Holman method with robust close-encounter detection algorithms, such as the Visser collision detection scheme, to enable accurate long-term simulations of densely populated or collisional systems.

In summary, this thesis demonstrates both the capabilities and limitations of the Wisdom–Holman integrator for long-term planetary dynamics. Its efficiency and stability for non-resonant systems make it a powerful tool for large-scale statistical studies, but special care is needed when simulating systems near resonance or with orbital crossings. The choice of coordinate system also plays a non-negligible role in long-term accuracy and should be considered alongside other numerical parameters. Addressing these challenges with improved algorithms and more adaptive methods will be critical for future advances in accurate and efficient celestial mechanics simulations.

10 Appendix

A Δt used for small time step limit

For the small Δt limit, the following values$\cdot 10^{-5}$ were used.

525	588	595	600	680	700
735	833	840	850	952	1020
1050	1176	1190	1225	1275	1400
1428	1666	1700	1785	1960	2040
2100	2380	2499	2550	2856	2940
2975	3400	3570	3675	4200	4760
4900	5100	5880	5950	7140	7350
8925	10200	11900	14280	14700	17850
19992	23800	29400	33320	41650	62475
71400	99960	166600	499800		

B Δt used for the larger time step intervals

For the broad Δt interval, the following values $\cdot\frac{1}{6}10^{-1}$ were used. For the super high Δt (and the examination of the error in the resonant system), the values were taken $\cdot\frac{1}{5}$.

1	2	3	4	5	6
7	8	10	12	14	15
17	20	21	24	25	28
30	34	35	40	42	49
50	51	56	60	68	70
75	84	85	98	100	102
105	119	120	136	140	147
150	168	170	175	196	200
204	210	238	245	255	280
294	300	340	350	357	392
408	420	425	476	490	510
525	588	595	600	680	700
714	735	833	840	850	952
980	1020	1050	1176	1190	1225
1275	1400	1428	1666	1700	1785
1960	2040	2100	2380	2499	2550
2856	2940	2975	3400	3570	3675
4200	4760	4900	5100	5880	5950
7140	7350	10200	11900	14280	14700
17850	19992	23800	29400	33320	41650
62475	71400	99960	166600	499800	

References

[1] C. D. Murray and S. F. Dermott. *Solar System Dynamics*. Cambridge University Press, 1999.

[2] E. Pardo. Asteroid 2023 dw: Can we deflect it if it threatens earth? March 14 2023.

[3] J. Wisdom and M. Holman. Symplectic maps for the n-body problem. *The Astronomical Journal*, 102(4):1528–1538, 1991.

[4] P. M. Visser. Collision detection for N-body Kepler systems. *Astronomy & Astrophysics*, 669:A97, jan 2023.

[5] M. J. Duncan, H. F. Levison, and M. H. Lee. A multiple time step symplectic algorithm for integrating close encounters. *The Astronomical Journal*, 116(5):2067–2077, 1998.

[6] R. Hanno and L. Shang-Fei. Rebound: an open-source multi-purpose n-body code for collisional dynamics. *Astronomy & Astrophysics*, 537:A128, January 2012.

[7] H. Rein and D. Tamayo. Whfast: a fast and unbiased implementation of a symplectic wisdom-holman integrator for long-term gravitational simulations. *MNRAS*, 452(1):376–388, 2015.

[8] NASA. Classical orbital elements. Retrieved from note = `https://nssdc.gsfc.nasa.gov/planetary/factsheet/sunfact.html`.

[9] Oikofuge. Keplerian orbital elements. 2022. Retrieved from `https://oikofuge.com/keplerian-orbital-elements/`.

[10] J. M. A. Danby. *Fundamentals of Celestial Mechanics*. Willmann-Bell, 2 edition, 1988.

[11] R. H. Battin. *An Introduction to the Mathematics and Methods of Astrodynamics*. American Institute of Aeronautics Astronautics, 1987.

[12] D. Jensen and S.C. Millholland. Inferred properties of planets in mean–motion resonances are biased by measurement noise. *The Astronomical Journal*, 164(4):183, 2022.

[13] NASA. Planetary fact sheet. Retrieved from `https://nssdc.gsfc.nasa.gov/planetary/factsheet/`.

[14] Astronomy Staff. How close does pluto's orbit come to neptune? *Astronomy*, February 2023. Retrieved from `https://www.astronomy.com/science/how-close-does-plutos-orbit-come-to-neptune/`.

[15] ThatsMaths. The 3:2 resonance between neptune and pluto. ThatsMaths (blog), dec 2018. Retrieved from `https://thatsmaths.com/2018/12/13/the-3-2-resonance-between-neptune-and-pluto/`.

[16] R. Malhotra and J.G. Williams. Pluto's heliocentric orbit. *Pluto and Charon*, 1997.

[17] E. Hairer et al. *Geometric Numerical Integration: Structure-Preserving Algorithms for Ordinary Differential Equations*, volume 31 of *Springer Series in Computational Mathematics*. Springer, 2 edition, 2006.

[18] J.M. Sanz-Serna. Symplectic integrators for hamiltonian problems: an overview. *Acta Numerica*, 3:243–286, 1994.

[19] H. Yoshida. Construction of higher order symplectic integrators. *Physics Letters A*, 150(5–7):262–268, 1990.

[20] J. R. Taylor. *Classical Mechanics*. University Science Books, Sausalito, California, 2005.

[21] K. Beuermann et al. Vlt observations of grb 990510 and its environment. *Astronomy & Astrophysics*, 352:L26–L30, August 1999.

[22] A. Nicuesa Guelbenzu et al. Grb090426: Discovery of a jet break in a short burst afterglow. *Astronomy & Astrophysics*, 531:L6, January 2011.

[23] P. Saha and S. Tremaine. Long-term planetary integration with individual time steps. *The Astronomical Journal*, 108(4):1962–1969, 1994.

[24] V. Emel'yanenko. A method of symplectic integrations with adaptive time-steps for individual hamiltonians in the planetary n-body problem. *Celestial Mechanics and Dynamical Astronomy*, 98:191–202, 2007.

[25] D. Viswanath. How many timesteps for a cycle? analysis of the wisdom–holman algorithm. *BIT Numerical Mathematics*, 42(1):194–205, 2002.